

Reassessing Exoplanet Light Curves with a Thermal Model

ARTHUR D. ADAMS¹ AND GREGORY P. LAUGHLIN¹

¹*Department of Astronomy, Yale University, New Haven, CT 06520*

Submitted to ApJ

ABSTRACT

We present a uniform assessment of existing near-infrared Spitzer Space Telescope observations of planet-bearing stars. Using a simple four-parameter blackbody thermal model, we analyze stars for which photometry in one or more of Spitzer’s bandpasses has been obtained over either a full, or a significant, fraction of the planetary orbit. Systems in this category comprise ten well-studied Hot Jupiters on circular or near-circular orbits (HAT-P-7, HD 149026, HD 189733, HD 209458, WASP-12, WASP-14, WASP-18, WASP-19, WASP-33, and WASP-43), as well as three stars harboring planets on significantly eccentric orbits (GJ 436, HAT-P-2, and HD 80606). We find that our simplified model can accurately reproduce the shape of the light curve in almost all cases, including the relative intensities of the minimum and maximum fluxes from the planets as well as the phase offsets of these extrema with respect to observed transits/secondary eclipses. For one notable exception, WASP-12 b, which is known to be tidally distorted, we add an additional parameter to account for its non-spherical shape. For a majority of the planets that we consider, full-orbit photometry is available in multiple wavelengths, allowing us to compare independent fits to the full- or extended-phase light curves obtained in different bands. In these cases, we find that the returned parameter values are largely in agreement, with two notable exceptions. The first is a disagreement in night-side temperature, suggesting distinct atmospheric layers, each with their own characteristic minimum temperature. The second is a diversity in albedos, suggesting variation in opacity of the atmospheric layers that generate the observed infrared emission. For instances where photometric light curves exist for multiple bands, we show that measured transit depths provides a consistency check for the accuracy of the photometric data reduction.

Keywords: atmospheric effects, methods: data analysis, methods: numerical, planets and satellites: atmospheres, planets and satellites: individual (GJ 436 b, HAT-P-2 b, HAT-P-7 b, HD 80606 b, HD 149026 b, HD 189733 b, HD 209458 b, WASP-12 b, WASP-14 b, WASP-18 b, WASP-19 b, WASP-33 b, WASP-43 b), techniques: photometric

1. INTRODUCTION

While planets on short orbital periods cannot be directly imaged, their orbital phases can often be inferred to high precision from transits and Doppler velocity measurements, and so the geometric conditions governing their time-dependent illumination phase functions can be known precisely. For the subset of planets that transit, a variety of observational strategies, including transmission and reflection spectroscopy – can be brought to the task of characterizing the planetary atmospheres. For the most well-studied planets, there is a broad consensus that measured emission spectra permit inferences of the molecular compositions and pressure-temperature profiles of the planetary at-

mospheres (Madhusudhan & Seager 2009; Madhusudhan et al. 2011). Data from observations have been used to support arguments for disequilibrium chemistry (Stevenson et al. 2010), thermal inversions (Knutson et al. 2008), and varying C/O ratios (Madhusudhan et al. 2011).

A primary result of observations over the last decade has been the detection of molecules, especially H₂O and CO, in exoplanet atmospheres. This work has been done primarily in the near-infrared, via ground- and space-based spectroscopy. The first claimed detection of CO was made in Snellen et al. (2010) for the well-studied planet HD 209458 b, using the spectrograph CRISES on the Very Large Telescope (VLT). While this particular

detection has not since been reproduced (Schwarz et al. 2015), a detection of CO in HD 189733 b was published in 2013 (Rodler et al. 2013). HD 209458 b has also showed spectral evidence of water (Beaulieu et al. 2010), and since 2010 several other planets, including GJ 1214 b (Berta et al. 2012), WASP-12, 17, and 19 (Mandell et al. 2013), and HD 189733 b (Crouzet et al. 2014) have shown spectral evidence of water in their transmission spectra.

Transmission spectra have revealed molecular signatures, but in many cases have also suggested the significant presence of clouds/hazes. Flatter than expected spectra have been observed in planets such as GJ 1214 b (Berta et al. 2012), GJ 3470 b (Crossfield et al. 2013). Additionally, clouds/hazes have been invoked to explain lower than expected signals of certain molecular species, due to the increased opacity of the atmosphere (Huitson et al. 2012; Evans et al. 2013; Mandell et al. 2013; Crouzet et al. 2014; Schwartz & Cowan 2015).

Within the framework of the theories of atmospheric composition and circulation, the effective albedo and heat recirculation/redistribution efficiency are the most robustly empirically constrained parameters. Their constraint often relies on the combination of measurements taken during both transit and secondary eclipse (Cowan & Agol 2011). The prediction that the day-night temperature contrast should increase with increasing equilibrium temperature is supported by calculations of the recirculation efficiencies for a number of Hot Jupiters (Wong et al. 2016). This trend is currently explained as a consequence primarily of atmospheric radiative heating/cooling (Komacek & Showman 2016).

Thermal inversion in the atmospheres of giant exoplanets is motivated both by the presence of an inversion layer in Jupiter’s atmosphere, as well as the relatively much stronger instellation for close-in giant planets that can drive such an inversion. Knutson et al. (2008) used eclipse observations of HD 209458 b in multiple Spitzer IRAC bands to suggest that atmospheric models with thermal inversion better explained the observed depths than models without inversion. These conclusions were consistent with the data, but came with acknowledgement that a truly robust determination of inversion layers would require more precise observations (Madhusudhan & Seager 2010). The evidence for inversion in HD 209458 b in particular has since been disputed (Diamond-Lowe et al. 2014; Schwarz et al. 2015; Line et al. 2016). Analyses of photometry from other planets have also suggested that the data are consistent with weak thermal inversions (Madhusudhan et al. 2011; O’Rourke et al. 2014). While the currently available data cannot broadly confirm the presence of thermal in-

versions, the expectation persists that inversion should exist in at least some subset of highly irradiated planets.

In stark contrast to the analyses that have presented evidence for atmospheric chemistry, inversions, and structural profiles, it has been argued, that in the majority of cases, the data are no more consistent within statistical uncertainty with a spectral retrieval model than with a simple blackbody radiative model (Hansen et al. 2014). This range in optimism of interpretation is quite striking, and has important implications for how the forthcoming observations of short period planets with JWST are to be interpreted.

In part, the disconnect that permits a startling range of interpretation can be ascribed to historical accident. The Spitzer Mission was designed and constructed prior to the discovery of transiting extrasolar planets (Werner 2006), and so its suite of instruments was not necessarily optimized for monitoring hot Jupiters and other short-period planets. Indeed, given that the Spitzer Space Telescope was not tuned for exoplanets, it is remarkable that some of the most exciting scientific results from the mission have come in connection with exoplanet-related observations.

Careful attention has been paid to the instrumental systematics in Spitzer data. The two major types of systematic effects are the detector “ramp”, a measurable brightening in time which has been observed in IRAC photometry, most notably at 8.0 μm (Deming et al. 2006; Grillmair et al. 2007; Knutson et al. 2008; Knutson et al. 2009; Désert et al. 2009; Agol et al. 2010; Todorov et al. 2010), and the “pointing oscillation” (Knutson et al. 2008; Deming et al. 2012; Todorov et al. 2014). Similar systematics appear to exist in the mid-infrared Spitzer MIPS instrument (Crossfield et al. 2012), limiting the constraint of light curve parameters. The properties of the instrumental effects on pixel-to-pixel and intra-pixel variability are now well-documented (Carey et al. 2012; Beichman et al. 2014), and various analyses have employed novel reduction techniques designed to address the known systematics (e.g. Diamond-Lowe et al. 2014; Todorov et al. 2014) and check the consistency of the results derived from the photometry (e.g. Ingalls et al. 2016). These considerations will certainly persist as we move to the next generation of space-based missions.

With Spitzer now in its sunset phases, and with JWST not yet on sky, there is a window of opportunity for a fresh assessment of the strengths of the various observational interpretations that have been offered. In this paper, we report the results of a uniform assessment of the existing secondary eclipse measurements and full- or extended-phase light curve photometry of close-in giant

planets. We argue that a simple 4-parameter model, which includes the planetary rotation rate, the time scale of atmospheric radiative response, the global planetary energy surface flux, and the planetary albedo can be used to characterize the observed planets at a level of detail that is matched consistently to the quality of the underlying data.

The plan of this paper is as follows. In §2, we review the current catalog of secondary eclipse measurements that have been carried out from ground and space. The conclusions of this analysis are used to motivate the presentation in §3, where we collect and discuss a normalized set of *Spitzer*’s full phase photometric measurements from various sources in the literature.

2. PHOTOMETRY

Broadband photometry offers a much lower-resolution but higher measurement signal-to-noise to study planet thermal emission. For a selection of planets orbiting relatively bright parent stars, photometry has been obtained throughout the orbit; such data are referred to as light curve observations. Full- or extended-phase photometry can be obtained through either fortuitous acquisition or planned observations. For example, the *Kepler* satellite returned data for a handful of planets that are hot enough or reflective enough to produce significant optical emission (Shporer 2017; Millholland & Laughlin 2017). The optical light curves of these planets were discerned after the primary transits were detected. In other cases, the *Spitzer Space Telescope* has made specifically targeted long-duration observations (sometimes lasting more than a week) of individual transiting planet bearing stars (Lewis et al. 2013).

The *Spitzer* mission, during both its cryogenic and “warm” phases, has obtained spectra, eclipse, transit, or full-phase observations of over 100 (check) planet-bearing stars. *Spitzer*’s IRAC detector (Werner et al. 2004) operates in 4 wavelength channels centered at 3.6, 4.5, 5.8, and 8.0 μm . During the “warm” phase, only the 3.6 and 4.5 μm were available. The Infrared Spectrograph (Houck et al. 2004) has provided spectra as well as photometry at 16 μm in the peak-up imaging mode, and the Multiband Imaging Photometer (MIPS) instrument (Rieke et al. 2004) provides photometry in the mid- to far infrared, particularly at 24 μm . All light curves analyzed in this work (listed in §2.2) were reduced and rebinned from data from the IRAC channels.

2.1. Secondary Eclipse Measurements

Full- or nearly full-phase light curve observations only exist for a small number of planets; a much larger sample of planets have had their secondary eclipse depths

measured. Secondary eclipses permit an assessment of the day-side temperatures and meteorological conditions. During the cryogenic phase of its mission, *Spitzer* observed 15 exoplanets in secondary eclipse in a selection of its 3.6, 4.5, 5.8, and 8 μm channels. Following depletion of its liquid helium, a substantial number of additional secondary eclipses at 3.6 μm and 4.5 μm have been detected, and at present, a total of 32 planets have eclipse depths measured. In total there are over 100 individual measurements made at bandpasses ranging from the *Kepler* optical band to ground-based measurements in J (1.22 μm), H (1.63 μm), and K (2.19 μm) (Croll et al. 2011).

A set of secondary eclipse measurements for a given planet at a range of different bandpasses amount to a low-resolution day-side emission spectrum of an extra-solar planet, and a handful of planets have been measured in five or more bands, including J, H, and K. Many planets furthermore, have been observed in three or more bands, and there has been a substantial effort to interpret the observational results with theoretical models. For example, Fortney et al. (2008) suggest that strongly irradiated atmospheres (corresponding roughly to the half of the observed planets that receive the largest orbit-averaged fluxes) have thermal inversions. Inversions are believed to arise from the presence of hardy molecules such as TiO or VO which absorb and re-radiate starlight at low pressures high in the atmosphere. A related class of models is presented by Burrows et al. (2008), which, in addition to varying the presence of a generic high-altitude gray absorber, also incorporate a heat sink added at depth to facilitate redistribution of heat from the planetary day-side to the night-side. Knutson et al. (2010) present evidence for empirical correlations which suggest that chromospheric activity inhibits the formation of such thermal inversions, perhaps by destroying the inversion-producing molecules through an elevated flux of high-energy photons. Madhusudhan (2012) as well as Madhusudhan & Seager (2010) have proposed that C/O ratios constitute a key dimension along which planets can exhibit planet-to-planet variation in secondary eclipse depths.

In the last several years developments in the reduction techniques for *Spitzer* photometry have led to re-analyses of existing data (e.g. Lewis et al. 2013; Todorov et al. 2013, 2014; Wong et al. 2014, 2015, 2016). With sufficient photometric signal-to-noise, finer structure in the eclipse can reveal features of the spatial intensity of the planet’s day-side (Rauscher et al. 2007). This manifests itself in variations of the ingress and egress, which can be interpreted using spherical harmonics in brightness on the planet’s visible disk (Majeau et al. 2012;

de Wit et al. 2012). In addition to single-eclipse profile variations, multiple observations of eclipses for a given planet over several years constrain not only the orbital period and ephemerides, but has led to measurements of orbital periastron precession (e.g. Wong et al. 2014).

A handful of planets on modestly to highly eccentric orbits have been observed during their eclipses, including GJ 436 b (Deming et al. 2007; Stevenson et al. 2010), HAT-P-2 b (Lewis et al. 2013), XO-3 b Wong et al. (2014), and HD 80606 b (Laughlin et al. 2009; de Wit et al. 2016). Since the atmospheres of eccentric planets undergo time-dependent instellation, in theory, the dynamics may be significantly different than those on circular orbits. For the two most eccentric cases (HAT-P-2 b and HD 80606 b), the orientation of their orbit with respect to our line of sight is such that periastron and secondary eclipse occur within intervals relatively short compared with their orbital periods, allowing us to measure valuable information about the intense day-side heating that occurs near periastron.

Figures 1–2 show distributions of the observed depth in units of the expected depth if the planet were uniformly radiating as a blackbody at its equilibrium temperature. A ratio considerably above unity suggests the planet is radiating much more strongly than would be expected from a blackbody at the planetary orbit-averaged equilibrium temperature, $\bar{T}_{\text{eq}} = T_{\text{eff}} \sqrt{R_{\star}/(2a)}$, where T_{eff} and R_{\star} are the effective temperature and radius of the host star, respectively, and a the orbital semi-major axis. Elevated flux ratios can be due to any number of factors spanning a variety of atmospheric and meteorological conditions.

We note the general trend in Figure 1 of increasing observed-to-thermal ratios with decreasing wavelength. For the bluest bands shown the highest observed fluxes are likely due to stronger contributions from reflected light. On the redder end, 13 eclipsing planets, or about 1/4 of the sample, have “sub-thermal” fluxes (ratios below unity). All are from Spitzer IRAC bands, and span equilibrium temperatures from 1142–1862 K. The minimum value of 0.63 occurs for WASP-17 b at 8.0 μm , with $\bar{T}_{\text{eq}} = 1547$ K.

Measurements of secondary eclipse depths for exoplanets are commonly reported in connection with comparisons to model spectra from model atmospheres of irradiated planets (e.g. Mahtani et al. (2013); Baskin et al. (2013)). The atmospheric models used for comparison often have a substantial degree of sophistication and are informed by multiple free parameters and physical assumptions. In most studies, some of the atmospheric parameters, such as the presence or absence of a high-altitude inversion-producing absorber, or the global av-

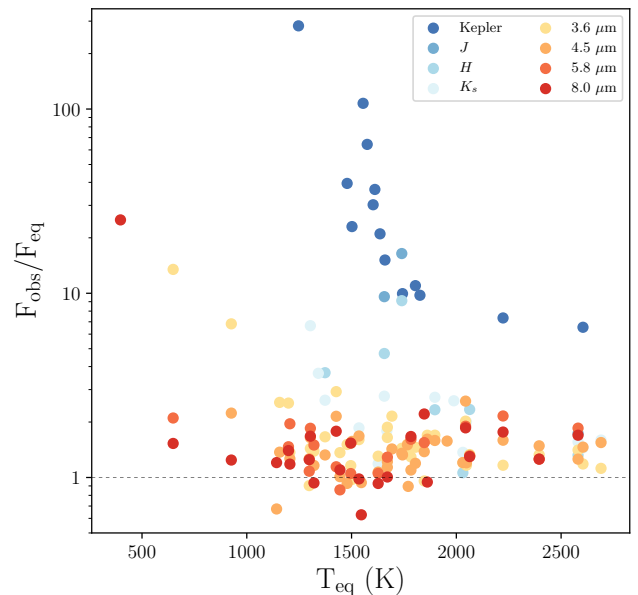


Figure 1. Collected secondary eclipse measurements of 53 planets, spanning one optical and seven infrared photometric bands. We plot the ratio, $F_{\text{obs}}/F_{\text{eq}}$ of the observed flux, F_{obs} , of the planet at secondary eclipse to the flux, F_{eq} that would result if the planet were a globally uniform blackbody radiating at the orbit-averaged equilibrium temperature, \bar{T}_{eq} . Values for $F_{\text{obs}}/F_{\text{eq}}$ generally exceed unity. This trend likely arises from inefficient transfer of heat from the day side to the night side, but can be attributed to a variety of additional contributions discussed in §2.1.

erage efficiency of day- to night-side heat redistributions are varied, whereas others, such as the assumption of hydrostatic equilibrium and global energy balance, are assumed settled.

Invariably, the number of implicit and explicit parameter choices substantially exceed the number of measurements, and make it difficult to evaluate the degree to which a given, highly detailed planetary atmospheric model exhibits explanatory power. The Central Limit Theorem states that any quantity that is formed from a sum of n completely independent random variables will approach a normal (Gaussian) distribution as $n \rightarrow \infty$. By extension, any quantity that is the product of a large number of random variables will be distributed approximately log-normally. To examine whether variations in eclipse fluxes exhibit this behavior, we fit the distributions of flux ratios with a log-normal probability distribution

$$f(x) = \frac{1}{\sqrt{2\pi} \sigma (x - x_0)} \exp \left\{ -\frac{1}{2} \left[\frac{\log(x - x_0) - \mu}{\sigma} \right]^2 \right\} \quad (1)$$

with free parameters x_0 , μ , and σ . Under the assumption the distribution is purely a product of strictly positive random variables, x_0 should theoretically be zero.

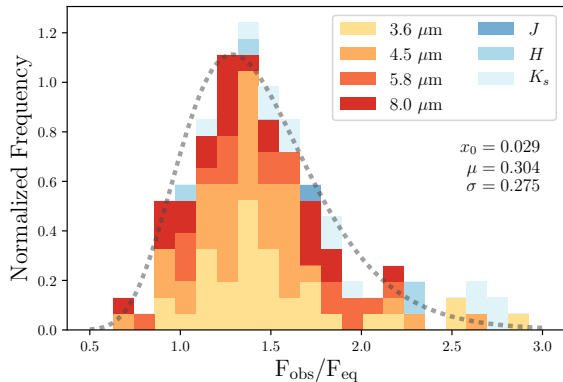


Figure 2. The stacked, normalized distribution of eclipse flux ratios in the Spitzer IRAC bands (warm colors) as well as JHK_s (cool colors) appears to follow a log-normal distribution (Equation 1). Note that we have truncated the histogram at a flux ratio of 3, but have included them in Figure 1.

The idea of comparing eclipse depths in two bands relative to the equilibrium depth was explored in [Baskin et al. \(2013\)](#). The day-side emission of close-in planets have been included in color-magnitude diagrams exploring whether Jupiter-size planets continue the trend of low-mass stars and brown dwarfs, behave similar to blackbodies, or neither ([Triaud et al. 2014](#)). In principle, we can combine elements of both approaches by using flux ratios relative to thermal in place of absolute magnitudes in a color-magnitude diagram. We construct flux “colors” by taking the difference in flux ratios of any two bands (Figure 3); we use the logarithms of flux ratios as an analogy to traditional magnitudes; .

2.2. Light Curve Measurements

Partial and full phase photometry in multiple channels exists for the 13 planets discussed in this work. This allows for empirical testing of evolutionary predictions of radiative models over a significant timeseries. For all except GJ 436 b and HD 209458b, Spitzer light curves in multiple bands are available, inviting analysis of the consistency (or lack of consistency) of the best-fit parameters in each wavelength.

The history of published phase photometry from Spitzer spans over a decade, starting with the publication of observations of a significant fraction of the orbit of HD 189733 b in 8.0 μm ([Knutson et al. 2007b](#)). Since phase variations can in principle offer valuable

evidence of atmospheric properties, publications of light curves often include analyses of the phase variations within the structure of radiative and dynamical models. In general, the sophistication of these models has developed over time, as more data and multiple bands become available. Models have ranged from analytical models that use a limited number of parameters incorporating thermal emission, ellipsoidal variations, and in some cases reflected light (e.g. [Knutson et al. 2007b](#); [Laughlin et al. 2009](#); [Cowan et al. 2012](#); [de Wit et al. 2016](#); [von Paris et al. 2016](#)), to fully 3-dimensional circulation models (e.g. [Showman & Guillot 2002](#); [Showman et al. 2009, 2015](#); [Lewis et al. 2010, 2014, 2017](#); [Dobbs-Dixon & Agol 2013](#); [Amundsen et al. 2016](#); [Komacek & Showman 2016](#)). We discuss the planet-specific histories of published full- or extended-phase light curves, and any models or predictions of properties of the planetary atmospheres accompanying the data. The order reflects the chronology of the earliest available phase photometry for each planet.

HD 189733 b: A significant fraction of the orbit in IRAC’s 8.0 μm band was published in 2007 ([Knutson et al. 2007a](#)). This early example of phase photometry includes both transit and eclipse, and allowed the authors to calculate a full range of brightness temperatures. The light curve also demonstrated a non-zero phase offset¹, which the authors conclude implies an eastward hotspot. [Knutson et al. \(2009\)](#) complement the previous light curve with another partial light curve in 24 μm . The phase offset and brightness temperatures are very similar in both 8.0 and 24 μm , the latter suggesting a vertical temperature homogenization (since the redder photosphere is expected to be at a deeper pressure). However, expectations of night-side methane abundances and equilibrium chemistry are inconsistent with both this conclusion and a high-altitude cloud cover. The authors conclude that efficient day-night heat transport is clear, but more complex phenomena will require better 1D and 3D modeling.

Nearly-full phase coverage is now also available in 3.6 and 4.5 μm ([Knutson et al. 2012](#)). The phase offsets for both the minima and maxima in these

¹ Phase offsets often refer to the offset in phase of the time of maximum flux with respect to the time of secondary eclipse. If the planet heats and cools instantaneously, one expects the highest flux at the “full” phase of observation, i.e. the time of eclipse. A sufficiently nonzero offset may indicate winds, a non-instantaneous radiative timescale, a combination, or possibly another set of factors.

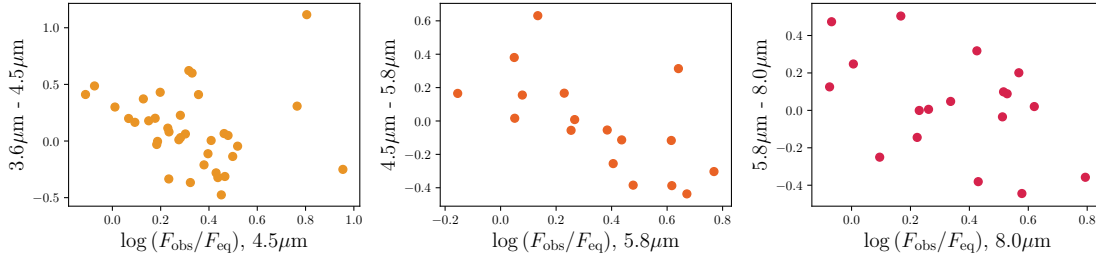


Figure 3. Eclipse color-magnitude diagrams are constructed by plotting the logarithm of the eclipse flux ratios in a given band (“magnitude”) versus the difference in logarithmic flux ratios between two bands (“color”).

bands are consistent with a coherent longitudinal wind, which was first suggested in the $8.0 \mu\text{m}$ data. On the instrumental side, [Knutson et al. \(2012\)](#) revisit the $8.0 \mu\text{m}$ phase data taking a more developed account of known instrumental systematic effects. They concede that the flux minimum in $8.0 \mu\text{m}$ could well be attributed to the detector “ramp” effect, rather than a physical phase offset.

Beyond this inference, the larger phase amplitude for $3.6 \mu\text{m}$ compared with $4.5 \mu\text{m}$ opposes the expectation from 1D models that redder wavelengths probe deeper atmospheric layers where temperatures variations are less severe. The addition of the bluer IRAC bands allows the authors to put forth a more coherent analysis of the carbon chemistry (CO and CH_4 primarily). From differences in transit depths between 3.6 and $4.5 \mu\text{m}$, they infer a possible excess in CO absorption. The corresponding full-phase light curves have a smaller amplitude of phase variations than what is predicted from 3D circulation models which assume equilibrium chemistry. From this [Knutson et al. \(2012\)](#) point to a possible disequilibrium: a vertical mixing of atmospheric layers on the planet’s night side, which could create an excess CO absorption signature.

HD 80606 b: [Laughlin et al. \(2009\)](#) presented roughly 30 hours worth of photometry at $8.0 \mu\text{m}$, encompassing the planet’s periastron passage. Given the orientation of the planet’s orbit relative to our line of sight, the secondary eclipse occurs just a few hours prior to periastron passage. [Laughlin et al. \(2009\)](#) attempted to fit a 2D hydrodynamical model with three free parameters (two for pressure of the photosphere, one for albedo) that are fixed at physically-motivated values. In the analysis they also assume a pseudo-synchronous rotation period of roughly 40 hours. They find a radiative time scale at $8.0 \mu\text{m}$ of 4.5 hours, which is

significantly shorter than the equivalent time scale on Earth. Given the assumed rotation rate and inferred radiative time scale, there is an expected decrease in flux following periastron which is not present in the model. From this the authors conclude there could either be efficient day-night heat advection, or a rotation period considerably different from pseudo-synchronous.

More recently, [de Wit et al. \(2016\)](#) present a new reduction of both the existing $8.0 \mu\text{m}$ photometry and newer $4.5 \mu\text{m}$ data which also include periastron and eclipse and span about 80 hours. They apply a simple radiative model with four parameters, similar to the one we employ for our current analysis, and find that HD 80606 b appears to rotate at a rate markedly slower than the theoretical pseudo-synchronous rate. The inferred radiative timescale of 4 hours is much shorter than the inferred rotation period.

Most recently, [Lewis et al. \(2017\)](#) have presented their own analysis of the 4.5 and $8.0 \mu\text{m}$ photometry, but with a fully 3D circulation model, and both constrain the rotation rate and invoke cloud/aerosol dynamics to explain variations in the light curves. Specifically, they tune the rotation in their model to the pseudo-synchronous rate, as well as one-half and twice the rate. The slowest rotation, with a period double pseudo-synchronous, gets closest to reproducing the amplitude of phase variations observed near periastron, though the phase offset moves slightly away from agreement with increasing period. Additionally, for the longer-baseline $4.5 \mu\text{m}$, including the effects of certain cloud species (most notably MgSiO_3) reduces the flux away from periastron which approaches the near-zero levels seen in the data.

HD 149026 b: Partial-phase photometry in $8.0 \mu\text{m}$ was published in [Knutson et al. \(2009\)](#), cover-

ing just under half an orbit. The light curve is comprised of 14 data points binned in 2.2-hour intervals (including one during eclipse). From this they employ a 2-hemisphere model (Cowan & Agol 2008) which models longitudinal variations in flux. Given the large uncertainties in the available data, they are not able to retrieve a phase offset statistically significant from zero.

Zhang et al. (2017) present their own recent reduction of phase photometry in 3.6 and 4.5 μm from 2011. Along with their analysis of WASP-33 b's photometry, their work uses calculated phase offsets to highlight a correlation between offset and the planet's orbit-averaged equilibrium temperature. The best-fit phase offsets from the 3.6 and 4.5 μm photometry are both significantly different from zero and in complete disagreement with each other. Given this disagreement, the authors point to potential systematic problems with the 3.6 μm data, whose offset is not supported by thermal models assuming synchronous rotation. These problems are not amenable to correction by any known algorithm at the pixel-to-pixel level, and even with a separate treatment for the systematics in the 3.6 μm data, the authors admit any inferences of phase offsets or variation amplitudes are unreliable.

WASP-12 b: Cowan et al. (2012) present full-phase light curves in both 3.6 and 4.5 μm . The authors uses sinusoids to model both the thermal and ellipsoidal variations, the latter of which is due to the expectation that the tidal distortion of the planet is significant enough to affect the shape of the phase curve. The measured transit depth at 3.6 μm is deeper than at 4.5 μm , implying a larger radius for the planet from the observed cross-section (i.e. along the day-night terminator). Since this is opposite the expectation of the thermal models considered in the paper, in order to explain the depth discrepancy the authors suggest the presence of a haze with a large scale height. Comparing the eclipse depths with 1-D radiative models, the authors find that their observations are consistent with an enhanced C/O ratio, but the uncertainties in the depths limit this to a marginal conclusion.

The ellipsoidal variations appear much more significant for the 4.5 μm data than at 3.6 μm . If physical, this implies the 4.5 μm photosphere occurs much higher in the planet's tidally distorted atmosphere. However, the authors point out that

there is a very real possibility that some uncharacterized detector systematics could explain much of the difference in strength of ellipsoidal variations between the two bands. Under this interpretation, the outermost, Roche-filling layers of the atmosphere would be optically thin.

WASP-18 b: Maxted et al. (2013) present full-phase light curves in both 3.6 and 4.5 μm . They employ a thermal model to explain modest phase variations, and note that in both bands, there appears to be uncharacterized systematic noise at the level of 10^{-4} in the flux ratio. They note that the amplitude of the WASP-12 b ellipsoidal variations at 4.5 μm presented in Cowan et al. (2012) are about an order of magnitude larger than the noise floor imposed by the systematics. Similar variations are not present in the 4.5 μm data for WASP-18 b.

HAT-P-2 b: HAT-P-2 b is currently the most comprehensively observed eccentric planet in photometry. Full phase data are available in both 3.6 and 4.5 μm , as well as partial coverage of both transit and eclipse in 8.0 μm (Lewis et al. 2013). Considering just eclipse depths, Lewis et al. (2013) find a best match to models which include high-altitude absorbers; however, an additional eclipse depth at 5.8 μm disagrees with such an interpretation. The light curves are compared with 1D radiative transfer models which assume instantaneous radiative timescales. The shape and phase offsets suggest a westward cool spot following transit, which is the opposite behavior from what one would expect for a super-rotating wind. Further analysis of the peak observed in 8.0 μm , which is higher than even the flux predicted with zero Bond albedo, suggest that chemistry and/or vertical temperature variations need to play a role in shaping the phase variations. The authors employ a sinusoidal model similar to that presented in Cowan & Agol (2008), but, accounting for the eccentric orbit, write the expected flux as a function of true anomaly rather than time. The consequence of such a model is that it implies the day-side brightness profile is constant, which is not expected from a physical standpoint for eccentric planets. The conclusion is that such a model fits the phase variations largely due to geometric effects from our line of sight.

HD 209458 b: The only full-phase light curve to date is in 4.5 μm , published in Zellem et al. (2014). The authors find their day-side flux is comparable with the results of the models presented in Showman et al. (2009). However, the models overesti-

mate the night-side flux; this disagreement is explained as a consequence of assuming equilibrium chemistry. In particular, a high abundance of CH_4 on the night-side could mitigate the difference between models and data. Beyond this, some systematics remain in the reduced data around secondary eclipse and near quadrature; [Zellem et al. \(2014\)](#) find it likely neither to be Spitzer pointing errors nor transit stellar variability. Given a similar systematic effect for HD 189733 b in 3.6 and 4.5 μm ([Knutson et al. 2012](#)), the authors conclude this is likely the result of some residual, uncharacterized Spitzer systematics.

GJ 436 b: [Lanotte et al. \(2014\)](#) present an analysis of a full-phase light curve in 8.0 μm in a paper which uses occultation depths spanning 3.6–24 μm to confirm previous inferences about the planet’s atmospheric composition. The authors compare the results from 3D circulation models from [Lewis et al. \(2010\)](#), which accounts for atmospheric metallicity and pseudo-synchronous rotation, with a fit assuming isotropic thermal emission. The [Lewis et al. \(2010\)](#) models need a metallicity much higher than solar to approach the thermal flux variations observed in the full-phase photometry. While their measured transit and eclipse depths at 3.6, 4.5, and 8.0 μm are shallower than preceding works, their conclusions about atmospheric chemistry are not affected qualitatively.

WASP-43 b: [Kataria et al. \(2015\)](#) compare broadband light curves from the Wide Field Camera WFC3 of the Hubble Space Telescope, as well as light curves from near-infrared bands ranging from 1.14–1.63 μm , with 3D atmospheric circulation models. The models predict a strong equatorial jet and are able to reproduce the peak day-side emission with a metallicity 5x solar. However, their model could not reproduce a low enough night-side flux to match the observed minimum. The authors suggest that either the night-side is brighter at lower effective temperatures, or that high-altitude clouds could play a role in limiting the observed flux.

More recently, [Stevenson et al. \(2017\)](#) have presented a sophisticated analysis of Spitzer 3.6 and 4.5 μm full-phase light curves. In their analysis, the metallicity of the atmosphere is consistent with solar, and they constrain the abundance of H_2O vapor on the day-side. In order to match the observed night-side fluxes, the authors include effects from clouds/hazes, though their results sug-

gest the cloud cover would need to be inhomogeneous. However, the authors note that their measured night-side fluxes at 3.6 μm were dependent on date of observation, which means the emission levels must be partially degenerate with some position-dependent Spitzer systematic.

WASP-14 b: [Wong et al. \(2015\)](#) present full-phase light curves in both 3.6 and 4.5 μm . While the 3D circulation models they adapt from the work of [Showman et al. \(2009\)](#) capture the day-side fluxes in both bands as intermediate to the models with and without TiO/VO absorbers, the night-side fluxes they predict disagree with the observed minima: the 3.6 μm minimum is over-predicted while the 4.5 μm is under-predicted. The authors point to an enhanced C/O ratio, or perhaps the presence of high-altitude silicate clouds, to explain both disagreements. Their dynamical model, the 3-D SPARC model [Showman et al. \(2009\)](#), assumes the modestly eccentric planet is rotating pseudo-synchronously, which is only slightly different from assuming spin-orbit synchronization.

HAT-P-7 b: [Wong et al. \(2016\)](#) present full-phase light curves in both 3.6 and 4.5 μm . Here their analysis of the eclipse depths lead to supporting a day-side thermal inversion with inefficient day-night heat redistribution. 1D and 3D model comparisons cannot explain the low night-side temperature in 3.6 μm . The authors suggest this is evidence for a high C/O ratio. HAT-P-7 b is also placed in the context of a trend of planets with relatively inefficient heat redistribution and high instellation. Even with a sophisticated correction for the Spitzer ramp as well as intrapixel and stellar variability, the authors note there still exists uncorrected noise in the 3.6 μm photometry.

In addition to Spitzer, [Armstrong et al. \(2016\)](#) present a phase curve from *Kepler* photometry in a recent analysis which suggests atmospheric variability in the atmosphere may be due to variable wind speeds causing variable cloud cover on the day-side. HAT-P-7 b is the first planet with phase photometry in both the optical and near-IR.

WASP-19 b: [Wong et al. \(2016\)](#) present full-phase light curves in both 3.6 and 4.5 μm . Unlike HAT-P-7 b, the authors find no evidence for a thermal inversion in the atmosphere; additionally, the day-night heat redistribution is more efficient. 1D and 3D model comparisons cannot explain the low night-side temperature in either band. The au-

thors suggest this discrepancy could be resolved by including high-altitude silicate clouds. Their analysis also places WASP-19 b within the trend of planets with increasingly inefficient redistribution with instellation.

WASP-33 b: Zhang et al. (2017) present their own recent reduction of full-phase photometry in 3.6 and 4.5 μm from 2012. As with HD 149026 b, the phase offset of WASP-33 b is used to suggest that observed phase offsets appear to correlate with equilibrium temperature. However, the uncharacterized systematics affecting the 3.6 μm light curve for HD 149026 b are not seen for WASP-33 b.

The analyses of Spitzer occultations and light curves has developed from just measurements of phase offsets and brightness temperatures in 8.0 μm , to inferences of thermal inversions, carbon chemistry, and optical absorbers with the addition of Warm Spitzer (3.6, 4.5 μm) photometry. Despite these advances in multi-wavelength photometry, no data are spared from persistent systematic effects in the Spitzer instrumental response, some of which appear to remain uncharacterized even in recent analyses. Additionally, 3-D modeling has not yet demonstrated a consistent ability to capture broad features of the available light curves, for example the amplitude of phase variations (e.g. HD 209458 b). The distribution of eclipse depths relative to the thermal expectation (§2.1) suggests we are encountering contributions from a potentially large number of physical processes, an interpretation which very well might extend to phase photometry. With this in mind, we put forth a physically rudimentary model in our current analysis (§4), to explore the limitation of sophistication of physical interpretation which might be imposed by the quality of Spitzer observations of exoplanets.

3. THE CASE FOR ECCENTRIC PLANETS

From a theoretical perspective, eccentric exoplanets will have atmospheric dynamics primarily driven by the stellar cycle, as opposed to smaller-scale effects. As an observational incentive, at fixed semimajor axis the geometric transit probability of an exoplanet increases with eccentricity.

3.1. Determining Rotation Rates

Rotation rates of gas giants in orbits close to their host stars (“*Hot Jupiters*”, or HJs) are currently not well-determined observationally. For sufficiently short-period planets, tidal locking (also known as synchronous rotation) is expected to occur on timescales shorter than the age of the system. The analogous case for close-in eccentric planets is the *pseudo-synchronous* rate, where the

planet effectively approximates tidal locking around periastron. Hut (1981) calculates the pseudo-synchronous rotation frequency as a function of eccentricity using a tidal argument, with the result

$$\Omega_{\text{PSR}} = \sqrt{\frac{a^3}{GM_\star}} \left[\frac{1 + \frac{15}{2}e^2 + \frac{45}{8}e^4 + \frac{5}{16}e^6}{(1 + 3e^2 + \frac{3}{8}e^4)(1 - e^2)^{3/2}} \right], \quad (2)$$

where a is the semimajor axis, M_\star the stellar mass, and e the orbital eccentricity. In the circular orbit limit ($e \rightarrow 0$), the spin frequency matches the orbital frequency, reaching tidal locking.

No strong empirical constraints yet exist for the rotation rates of any eccentric exoplanets, let alone Hot Jupiters. de Wit et al. (2016) have recently calculated the rotation rate of the extremely eccentric HD 80606 b as 93^{+85}_{-35} hours, which is inconsistent with the theoretical pseudo-synchronous period of 39.9 hours. While a deviation from synchronous rotation could be explained in circular-orbit Hot Jupiters as a presence of a bulk equatorial flow, it is not known whether this phenomenon exists in general for eccentric planets.

3.2. Kozai-Lidov Mechanism

In a 3-body system consisting of a close binary accompanied by a third outer perturbing body, the Kozai-Lidov mechanism (Kozai 1962; Lidov 1962) represents a process by which the orbital eccentricity of the inner binary may be stimulated. The mechanism “trades” mutual inclination of the outer body’s orbit and the inner binary with the eccentricity of the inner binary, in periodic cycles known as *Kozai cycles*.

The idealized picture can be extended to a more realistic scenario when one considers the inner binary bodies as extended objects rather than point masses. Eggleton & Kiseleva-Eggleton (2001) consider both the distortion effects on the inner objects due to their spins and mutual gravity, as well as the orbital evolution due to tidal friction and general relativistic effects. Wu & Murray (2003) apply this physical framework to the known properties of the binary system HD 80606/80607, a wide binary (~ 1000 AU) system of two solar-type stars with one known exoplanet orbiting one of the stars (HD 80606) in a highly eccentric orbit. Fabrycky & Tremaine (2007) generalize this theory (Kozai Cycles with Tidal Forces, or KCTF) to both explain the prevalence of gas giants in close orbits and create a testable prediction of the statistical occurrence rates of highly inclined binary systems which host planets.

3.3. Tidal Evolution

Planets on eccentric orbits are predicted through tidal evolution to circularize their orbits on a timescale com-

monly known as the *circularization timescale* (Goldreich & Soter 1966; Rasio et al. 1996), given by

$$\tau_e = \frac{4}{63} Q \sqrt{\frac{a^3}{GM_\star}} \left(\frac{M_P}{M_\star} \right) \left(\frac{a}{R_P} \right)^5 \quad (3)$$

where the *specific dissipation function* Q is a parameter that encapsulates the ability of the planet, given its internal structure and rheology, to dissipate tidal forces via internal heating. For reference, estimates from Lainey et al. (2009) place Jupiter at $Q_J \sim 3 \times 10^4$. Compare this with HD 80606 b, whose tidal dissipation efficiency is estimated to be much lower, at $Q > 2.5 \times 10^6$ (de Wit et al. 2016); hence, HD 80606 b is able to sustain a highly eccentric orbit for a timescale at least comparable with the age of its host star.

4. BLACKBODY THERMAL MODEL

Our analysis begins with published properties of exoplanet systems (Table 1). In particular, the orbital geometries of all systems considered are incredibly well-constrained, with fractional uncertainties at a maximum of 10^{-5} in period and 10^{-3} in eccentricity.

We begin by modeling the planet using a latitude/longitude grid with cells of dimension $5^\circ \times 5^\circ$. Each cell is modeled as a blackbody, with the thermal energy set by a combination of time-dependent instellation and a parametrized baseline temperature which attempts to capture, to first-order, heating from the planet interior (see Section 4.1). Advection is not modeled; instead the model uses a bulk rotation parameter that does not and cannot distinguish between differential rotation of radiating material and a coherent solid-body rotation.

The evolution of grid cell temperatures in time is combined with the known geometry of the orbit with respect to the observer and instrumental bandpasses to generate model full-orbit light curves for a given set of parameter values, which can be adjusted to fit the data.

4.1. Model Parameters

We attempt to fit several exoplanetary light curves from the *Spitzer Space Telescope* with a simple 4-parameter blackbody radiative model. Each parameter captures a broad physical property of the planet.

Rotation Period (P_{rot}): Coherent rotation of the planet is often parametrized in units of either the orbital period (for circular orbits) or the theoretical pseudo-synchronous rate (for eccentric orbits). This parameter may also equivalently represent a coherent velocity of an atmospheric layer probed by a specific wavelength.

Radiative Timescale (τ_{rad}): The radiative timescale determines how quickly parcels of material change temperature in response to instellation. In general the rate of change depends both on this parameter as well as the equilibrium temperature. The equilibrium temperature is dependent on time-dependent properties like the star-planet separation and local stellar altitude (Equation 5). Therefore, for the purposes of our analysis we choose to report our results in terms of the corresponding radiative timescale τ_{eq} at a reference temperature of the orbit-averaged equilibrium temperature.

Minimum (“Night-Side”) Temperature (T_0): All heat sources other than instellation (e.g. tidal heating, internal thermal processes) contribute to the minimum temperature.

Albedo (A): The scaling of the fraction of incident stellar flux absorbed allows us to account for a mean global reflectivity due to cloud cover. This parameter represents a characteristic Bond albedo.

This formulation allows us to model the largest-scale features observed in the *Spitzer* light curves. Most prominently, as shown in detail for planets such as HD 189733b (Knutson et al. 2007a, 2009, 2012) and HD 209458b (Zellem et al. 2014), observed times of minimum/maximum flux occur noticeably prior to transit/secondary eclipse, respectively. This corroborates a phenomenon commonly known as an “eastward hotspot” which has been demonstrated in global atmospheric simulations; a careful summary of such simulations is detailed in Zellem et al. (2014). The ability for our model to effectively model this offset in extrema depends on both a non-synchronous rotation period parameter value (for circular orbits), coupled with a radiative timescale on order the rotation period. In the limit $\tau_{\text{eq}} \ll P_{\text{rot}}$, the offset will vanish as cells respond thermally much more quickly than they are advected longitudinally into the view of the observer.

4.2. Thermal Evolution

The planet model is initialized with a uniform surface temperature T_0 . For eccentric orbits, the planet is initialized at apastron. At each successive point in time the change in temperature of each cell is calculated as

$$\dot{T}(\phi, \theta, t) = \frac{T_{\text{eq}}(\phi, \theta, t)}{4\tau_{\text{rad}}} \left\{ 1 - \left[\frac{T(\phi, \theta, t)}{T_{\text{eq}}} \right]^4 \right\} \quad (4)$$

Table 1. Orbital and Stellar Properties for Exoplanets with Spitzer Light Curves

Name	P (days)	e	ω ($^\circ$)	Ref.	M_* (M_\odot)	R_* (R_\odot)	T_{eff} (K)	Ref.
GJ 436 b	$2.64389803^{+0.00000027}_{-0.00000025}$	$0.1616^{+0.0041}_{-0.0032}$	$327.2^{+1.8}_{-2.2}$	1	$0.556^{+0.071}_{-0.065}$	0.455 ± 0.018	3416 ± 54	2
HAT-P-2 b	$5.6334729 \pm 6.1 \times 10^{-6}$	0.5171 ± 0.0033	185.22 ± 0.95	3	1.36 ± 0.04	$1.69^{+0.09}_{-0.08}$	6290 ± 60	3
HAT-P-7 b	$2.2047372 \pm 1.1 \times 10^{-6}$	$0.0016^{+0.0034}_{-0.0010}$	165^{+93}_{-66}	4	$1.47^{+0.08}_{-0.05}$	1.84 ± 0.17	6441 ± 69	5, 6
HD 80606 b	$111.43740 \pm 7.2 \times 10^{-4}$	$0.93286 \pm 5.5 \times 10^{-4}$	300.83 ± 0.15	7	1.007 ± 0.024	1.01 ± 0.05	5574 ± 50	8, 9
HD 149026 b	$2.8758911 \pm 2.5 \times 10^{-6}$	~ 0	N/A	10	1.345 ± 0.020	$1.541^{+0.046}_{-0.042}$	6160 ± 50	10
HD 189733 b	$2.218575200 \pm 7.7 \times 10^{-8}$	~ 0	N/A	11	0.846 ± 0.049	0.805 ± 0.016	4875 ± 43	12, 13
HD 209458 b	$3.52474859 \pm 3.8 \times 10^{-7}$	~ 0	N/A	14	$1.131^{+0.026}_{-0.024}$	1.203 ± 0.061	6092 ± 103	13, 15
WASP-12 b	$1.09142119 \pm 2.1 \times 10^{-7}$	0.0447 ± 0.0043	$272.7^{+2.4}_{-1.3}$	16, 17	1.280 ± 0.05	1.630 ± 0.08	6300^{+200}_{-100}	18, 19
WASP-14 b	$2.24376524 \pm 4.4 \times 10^{-7}$	~ 0	N/A	20	1.392 ± 0.040	1.004 ± 0.016	5568 ± 71	21
WASP-19 b	$0.788838989 \pm 4.0 \times 10^{-8}$	$0.0020^{+0.0140}_{-0.0020}$	259^{+13}_{-170}	4	0.904 ± 0.040	1.004 ± 0.016	5568 ± 71	22, 6
WASP-33 b	$1.2198669 \pm 1.2 \times 10^{-6}$	~ 0	N/A	23	1.495 ± 0.031	1.444 ± 0.034	7430 ± 100	23
WASP-43 b	$0.81347753 \pm 7.1 \times 10^{-7}$	$0.0035^{+0.0060}_{-0.0025}$	328^{+115}_{-34}	24	1.036 ± 0.019	$0.667^{+0.011}_{-0.010}$	4520 ± 120	24

References—(1) Maciejewski et al. (2014); (2) von Braun et al. (2012); (3) Pál et al. (2010), Lewis et al. (2013); (4) Wong et al. (2016); (5) Pál et al. (2008) (M_* , R_*); (6) Torres et al. (2012) (T_{eff}); (7) Winn et al. (2009a); (8) Hébrard et al. (2010) (M_* , R_*); (9) Moutou et al. (2009) (T_{eff}); (10) Carter et al. (2009); (11) Baluev et al. (2015); (12) de Kok et al. (2013) (M_*); (13) Boyajian et al. (2015) (R_* , T_{eff}); (14) Knutson et al. (2007b); (15) Takeda et al. (2007) (M_*); (16) Turner et al. (2016) (P , e); (17) Knutson et al. (2014) (ω); (18) Enoch et al. (2010); (19) Hebb et al. (2009); (20) Wong et al. (2015); (21) Joshi et al. (2009); (22) Tregloan-Reed et al. (2013) (M_* , R_*); (23) Collier Cameron et al. (2010); (24) Gillon et al. (2012).

where the equilibrium temperature can be calculated at a given point in the orbit via

$$T_{\text{eq}}^4(\phi, \theta, t) = (1 - A) \left[\frac{L_*}{4\pi\sigma r(t)^2} \right] \alpha(\phi, \theta, t) + T_0^4. \quad (5)$$

Here $r(t) = a[1 - e \cos E(t)]$ is the star-planet separation and is calculated numerically via Kepler's equation

$$M(t) = E(t) - e \sin E \quad (6)$$

where $E(t)$ is the eccentric anomaly and $M(t) = 2\pi(t - t_{\text{per}})/P_{\text{rot}}$ for periastron passage time t_{per} .

α is the attenuation factor of instellation due to the apparent altitude of the star at a particular cell on the planet surface, and can be calculated from the longitude ϕ , latitude θ , rotation period, and true anomaly $\nu(t)$ as

$$\alpha(\phi, \theta, t) = \cos \left\{ \phi - \left[\frac{2\pi t}{P_{\text{rot}}} + \nu(t) \right] \right\} \cos \theta. \quad (7)$$

5. APPLICATION TO KNOWN EXOPLANETS

5.1. Generating Light Curves from the Thermal Model

For a given set of parameters, one evolves the thermal model through successive orbits until the temperatures

(and hence resulting light curves) are visibly consistent from one orbit to the next. In practice this is achieved in just a few orbits. The results from the final orbit of each model is used to fit to the data.

To generate model light curves from temperature maps, we note that each cell has a specific radiative intensity given by its blackbody temperature. Then, integrating over the hemisphere of the planet that would be visible to the observer given the known orbital geometry, we can calculate the total observed flux at a given wavelength. Integrating these fluxes over the filter profile of the Spitzer IRAC bands, we generate planet-star contrast ratios (light curves) over a full orbit.

5.2. Statistical Methods

We sample parameter space uniformly over physically feasible ranges in each, and calculate Gaussian likelihoods in each to get a sense of the landscape of likelihoods. An annealing Metropolis-Hastings algorithm allows us to use Markov-Chain Monte Carlo techniques to rapidly find an optimal likelihood. In order to quantify the uncertainty in the parameters we run new MCMC chains without annealing, starting at points in parameter space corresponding to the using the 68% ranges of explored values on either side of the best-fit parameter values to define 1σ uncertainties.

Table 2. Best-Fit Parameters from Radiative Model

Planet	λ (μm)	P_{rot}		τ_{eq} (hr)	T_0 (K)	A
		(P_{PSR})	(days)			
GJ 436 b	8.0	$0.46^{+0.08}_{-0.16}$	$1.05^{+0.18}_{-0.37}$	$4.3^{+17.4}_{-2.4}$	616^{+49}_{-78}	$0.19^{+0.11}_{-0.11}$
HAT-P-2 b	3.6	$0.78^{+0.01}_{-0.27}$	$1.48^{+0.02}_{-0.52}$	$2.2^{+5.5}_{-1.2}$	1200^{+128}_{-118}	< 0.19
	4.5	$0.83^{+0.50}_{-0.04}$	$1.57^{+0.94}_{-0.08}$	$0.3^{+24.2}_{-N/A}$	1832^{+61}_{-55}	$0.42^{+0.15}_{-0.10}$
	8.0	$1.25^{+0.18}_{-0.37}$	$2.36^{+0.33}_{-0.71}$	$0.3^{+3.5}_{-0.2}$	918^{+133}_{-472}	< 0.06
HAT-P-7 b	3.6	$1.04^{+0.04}_{-0.01}$	$2.29^{+0.08}_{-0.03}$	$24.0^{+11.0}_{-16.4}$	177^{+425}_{-86}	< 0.05
	4.5	$1.19^{+0.08}_{-0.04}$	$2.62^{+0.19}_{-0.10}$	$12.1^{+8.8}_{-6.6}$	2043^{+52}_{-37}	$0.11^{+0.09}_{-0.04}$
HD 80606 b	4.5	$0.74^{+0.18}_{-0.37}$	$1.24^{+0.30}_{-0.62}$	$0.6^{+27.9}_{-0.4}$	561^{+182}_{-427}	$0.67^{+0.06}_{-0.15}$
	8.0	$1.23^{+0.01}_{-0.34}$	$2.05^{+0.02}_{-0.56}$	$3.9^{+15.8}_{-1.9}$	930^{+68}_{-281}	$0.85^{+0.05}_{-0.16}$
HD 149026 b	3.6	$1.11^{+0.05}_{-0.05}$	$3.18^{+0.15}_{-0.15}$	$97.0^{+19.3}_{-11.9}$	1192^{+234}_{-225}	$0.01^{+0.10}_{-0.01}$
	4.5	$0.51^{+0.28}_{-0.03}$	$1.47^{+0.80}_{-0.09}$	$4.1^{+12.3}_{-2.3}$	1354^{+101}_{-187}	$0.57^{+0.06}_{-0.09}$
HD 189733 b	3.6	$0.68^{+0.05}_{-0.10}$	$1.52^{+0.11}_{-0.23}$	$17.2^{+3.6}_{-5.3}$	982^{+18}_{-64}	$0.17^{+0.03}_{-0.10}$
	4.5	$0.73^{+0.32}_{-0.05}$	$1.62^{+0.70}_{-0.10}$	$6.7^{+7.2}_{-4.6}$	1094^{+23}_{-13}	$0.60^{+0.05}_{-0.01}$
	8.0	$0.79^{+0.06}_{-0.28}$	$1.75^{+0.13}_{-0.62}$	$0.3^{+4.0}_{-0.2}$	1181^{+10}_{-24}	$0.64^{+0.02}_{-0.04}$
HD 209458 b	4.5	$0.46^{+0.20}_{-0.03}$	$1.63^{+0.71}_{-0.12}$	$9.9^{+10.0}_{-0.8}$	1036^{+67}_{-30}	$0.26^{+0.08}_{-0.03}$
WASP-12 b	3.6	$0.69^{+0.22}_{-0.01}$	$0.74^{+0.24}_{-0.01}$	$8.1^{+34.7}_{-0.8}$	465^{+1277}_{-52}	< 0.02
	4.5	$0.95^{+0.01}_{-0.01}$	$1.02^{+0.01}_{-0.01}$	$34.6^{+6.8}_{-6.6}$	2259^{+22}_{-21}	< 0.03
WASP-14 b	3.6	$1.03^{+0.05}_{-0.07}$	$2.22^{+0.12}_{-0.15}$	$2.8^{+11.8}_{-1.5}$	1243^{+63}_{-80}	< 0.04
	4.5	$1.12^{+0.16}_{-0.07}$	$2.41^{+0.34}_{-0.16}$	$4.5^{+1.9}_{-2.7}$	1694^{+50}_{-27}	$0.18^{+0.09}_{-0.03}$
WASP-18 b	3.6	$1.05^{+0.07}_{-0.03}$	$0.98^{+0.07}_{-0.02}$	$7.8^{+10.6}_{-4.4}$	1556^{+85}_{-67}	< 0.04
	4.5	$1.05^{+0.09}_{-0.01}$	$0.99^{+0.09}_{-0.01}$	$10.2^{+1.6}_{-6.7}$	1519^{+47}_{-49}	< 0.01
WASP-19 b	3.6	$0.96^{+0.01}_{-0.02}$	$0.76^{+0.01}_{-0.02}$	$9.5^{+5.3}_{-3.7}$	1366^{+30}_{-28}	$0.09^{+0.02}_{-0.03}$
	4.5	$0.95^{+0.01}_{-0.01}$	$0.75^{+0.01}_{-0.01}$	$10.8^{+2.4}_{-2.4}$	1403^{+21}_{-25}	$0.10^{+0.03}_{-0.02}$
WASP-33 b	3.6	$0.96^{+0.08}_{-0.08}$	$1.17^{+0.10}_{-0.10}$	$4.7^{+3.9}_{-3.3}$	2336^{+42}_{-38}	$0.55^{+0.05}_{-0.04}$
	4.5	$0.61^{+0.00}_{-0.20}$	$0.74^{+0.00}_{-0.25}$	$2.3^{+0.3}_{-0.7}$	2171^{+14}_{-126}	$0.43^{+0.01}_{-0.12}$
WASP-43 b	3.6	$0.94^{+0.03}_{-0.03}$	$0.76^{+0.03}_{-0.02}$	$3.1^{+1.6}_{-1.6}$	434^{+48}_{-130}	$0.04^{+0.02}_{-0.02}$
	4.5	$0.97^{+0.01}_{-0.01}$	$0.79^{+0.00}_{-0.01}$	$14.1^{+3.8}_{-3.4}$	847^{+30}_{-37}	$0.23^{+0.01}_{-0.03}$

NOTE—The parameter values from our blackbody model returning the most favorable likelihood from MCMC algorithms. Uncertainties listed are 1σ ranges of a Metropolis-Hastings algorithm walk around the region of most favorable likelihood in parameter space.

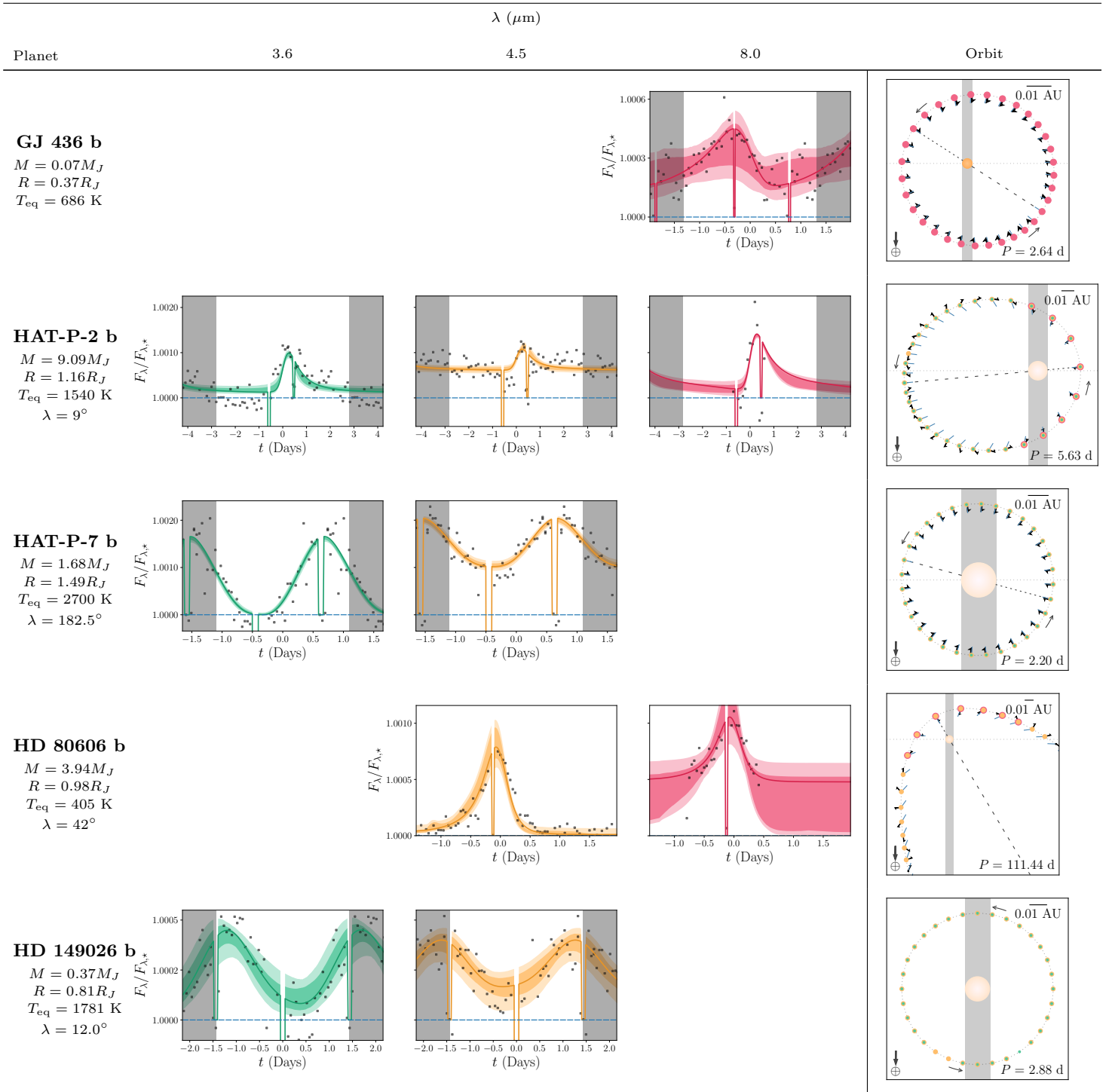
Table 3. Model Light Curves and Orbital Diagrams*Table 3 continued*

Table 3 (continued)

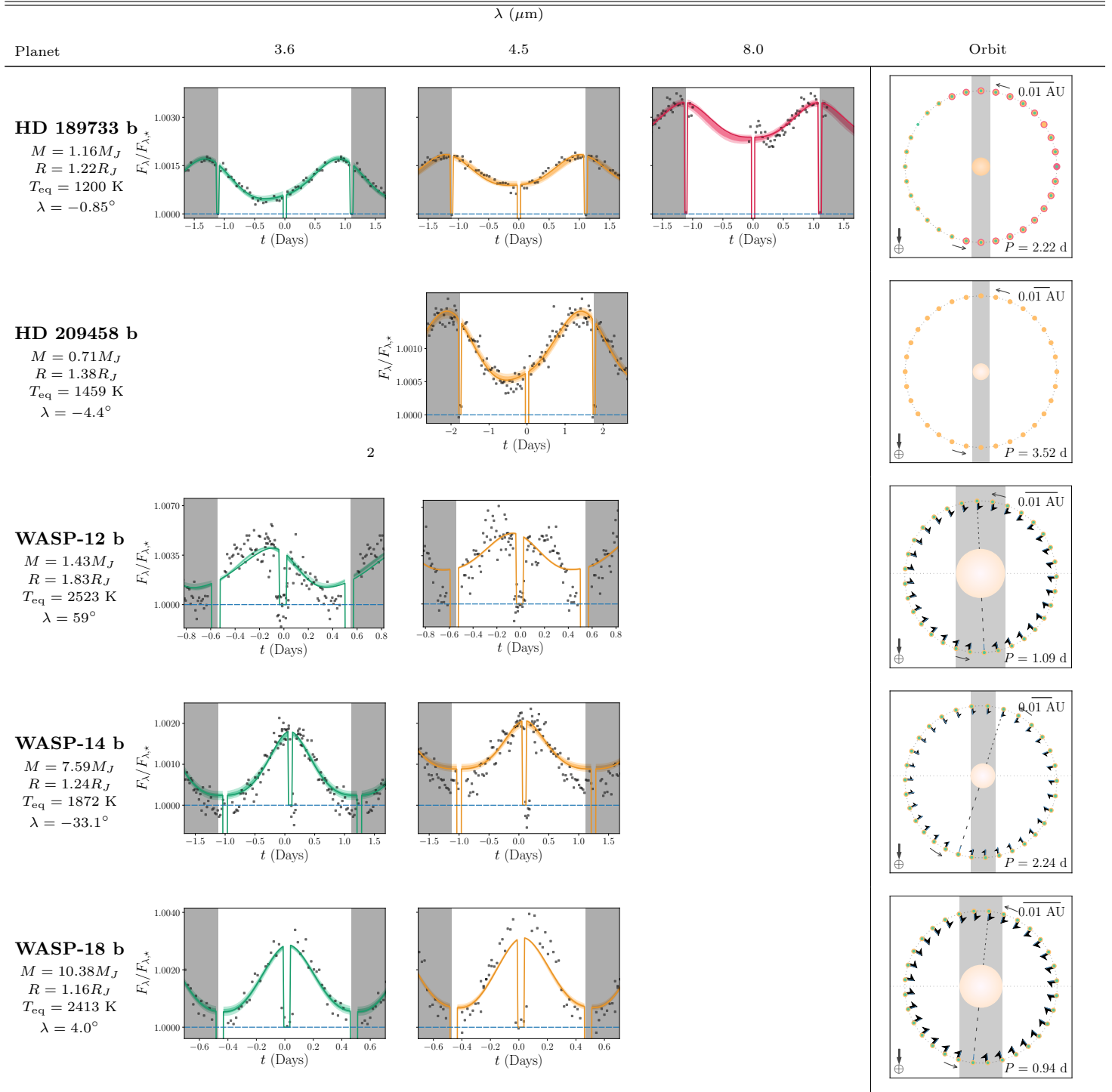
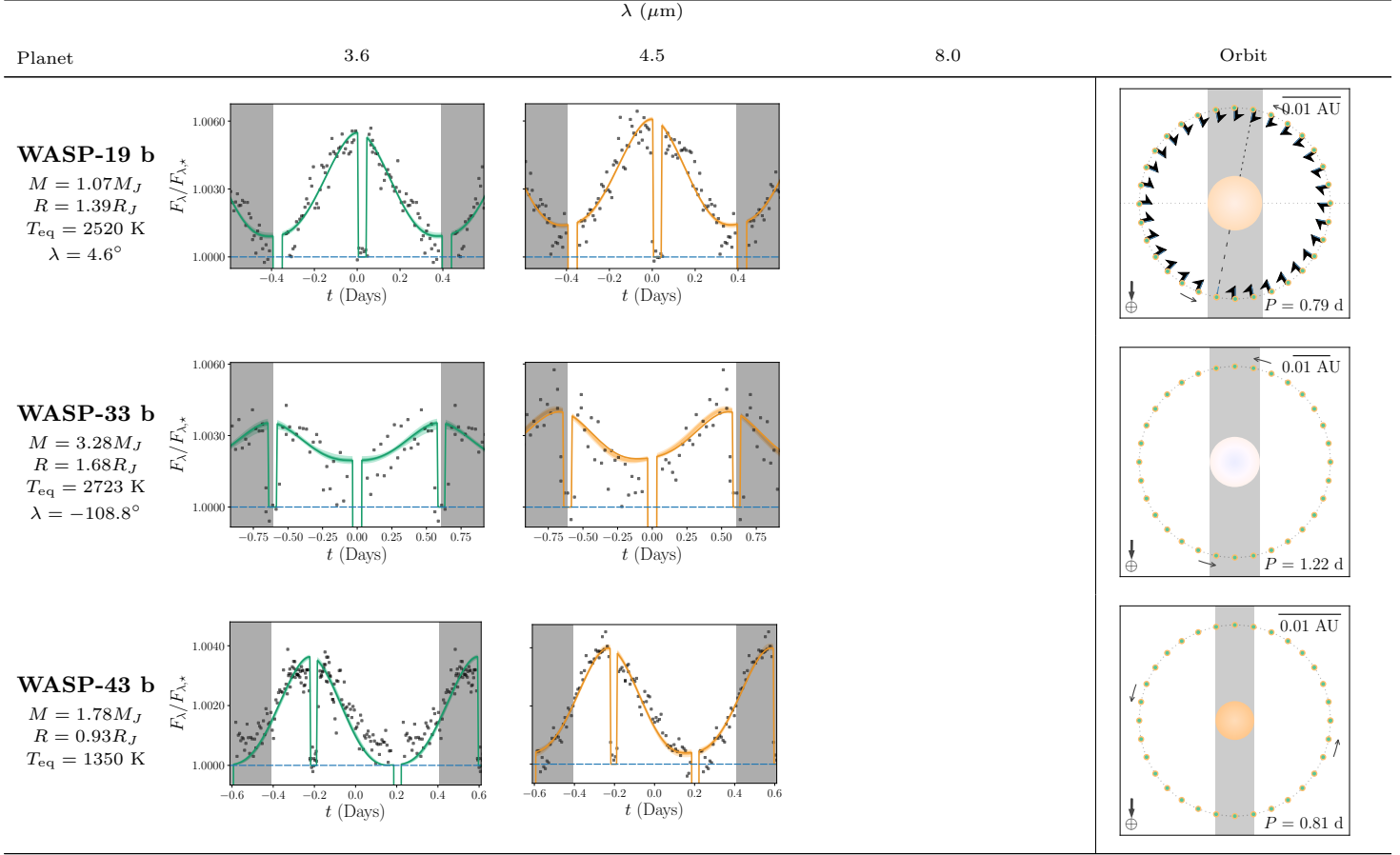


Table 3 continued

Table 3 (continued)



References—*Planet properties:* Turner et al. (2016) (GJ 436 b), Pál et al. (2010) (HAT-P-2 b), Wong et al. (2016) (HAT-P-7 b), Pont et al. (2009) (HD 80606 b), Carter et al. (2009) (HD 149026), Southworth (2010) (HD 189733 b, HD 209458 b), Southworth (2012) (WASP-12 b), Raetz et al. (2015) (WASP-14 b), Southworth (2012) (WASP-18 b), Wong et al. (2016) (WASP-19 b), Turner et al. (2016) (WASP-33 b), Hellier et al. (2011a) and Salz et al. (2015) (WASP-43 b). *Spin-orbit misalignments:* Albrecht et al. (2012) (HAT-P-2 b), Winn et al. (2009b) (HAT-P-7 b), Hébrard et al. (2010) (HD 80606 b), Albrecht et al. (2012) (HD 149026 b), Triaud et al. (2009) (HD 189733 b), Winn et al. (2005) (HD 209458 b), Albrecht et al. (2012) (WASP-12 b), Johnson et al. (2009) (WASP-14 b), Triaud et al. (2010) (WASP-18 b), Hellier et al. (2011b) (WASP-19 b), Collier Cameron et al. (2010) (WASP-33 b).

5.3. Circular Orbit Hot Jupiters

5.3.1. HAT-P-7 b

The best fits in both bands agree quite well in preferred rotation period. The $3.6 \mu\text{m}$ model is marginally consistent with spin synchronization, and slightly longer in the $4.5 \mu\text{m}$ model. The models also agree on a radiative timescale within 1σ , and disagree only slightly on albedo, with the $3.6 \mu\text{m}$ model preferring effectively zero albedo and the $4.5 \mu\text{m}$ model retaining a modest non-zero albedo. The night-side temperatures differ significantly within uncertainties, with the $3.6 \mu\text{m}$ model returning a minimum temperature effectively consistent with zero, and the $4.5 \mu\text{m}$ model returning a significant minimum temperature exceeding 2000 K.

We construct a check on the consistency of the photometry among bands of a single planet, which we high-

light using HAT-P-7 b (Figure 4). We take the sampled photometry which lie within the transit and shift them up by the geometric transit depth. Assuming the differences in opacities of the atmosphere at each wavelength do not contribute significantly to the observed transit depth, we expect the resulting flux levels to be at least marginally consistent.

5.3.2. HD 149026 b

Only the night-side temperatures for the 3.6 and $4.5 \mu\text{m}$ models agree within 1σ . While the light curves both have muted amplitudes relative to the instantaneously and completely re-radiating case, the models prefer different means of recreating the shallow variations. In the $3.6 \mu\text{m}$ model, a very long radiative timescale is preferred, with a very small albedo. The $4.5 \mu\text{m}$ model, in contrast, a short radiative timescale is paired with a

HAT-P-7 b

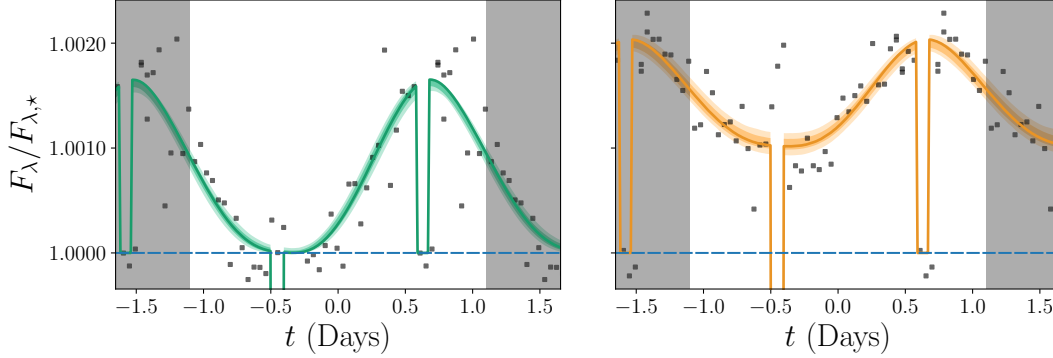


Figure 4. If differences in the opacities between IRAC bands can be neglected, the transit depths in each band should be marginally consistent. We visualize this by adding back the geometric transit depth to the binned photometry within the observed transit. Here we present similar light curves as in Table 3, but with the in-transit and in-eclipse shifted by the geometric depth. The resulting points are marginally consistent for $3.6 \mu\text{m}$, but noticeably higher for $4.5 \mu\text{m}$, indicating a clear difference in the transit depths by wavelength.

quite high albedo, absorbing only half of the incident stellar radiation.

Beyond these disagreements, the light curves also disagree visibly with respect to the observed phase offsets. The $4.5 \mu\text{m}$ light curve exhibits a slight positive phase offset, which we model with a rotation rate faster than synchronous. However, the $3.6 \mu\text{m}$ data appear to have a flux minimum which follows, rather than precedes, the transit. Therefore, the model returns a rotation rate slower than synchronous.

5.3.3. *HD 189733 b*

Both the 3.6 and $4.5 \mu\text{m}$ light curves exhibit minima in the flux which occur prior to the transits. Accordingly, the rotation periods in each wavelength are consistent both with each other and with a planet whose relevant photospheres are super-rotating² All three night-side temperatures disagree within uncertainties. This is not surprising with respect to the 8.0μ data which are elevated entirely above either of the other light curves, suggesting a significant discrepancy in the temperatures of the material responsible for emission at each band. The albedos in each wavelength are also both significantly nonzero and inconsistent with each other, pointing to further evidence of distinct photospheres with distinct properties such as temperature and opacity.

5.3.4. *HD 209458 b*

The model is consistent with the observed pre-transit minimum in the flux curve within the model uncertain-

ties. This is accomplished by both relaxing the assumption of a synchronous rotation period and having a radiative time scale which is non-negligible compared with the rotation period. Here we find a best-fit rotation period that is ~ 0.46 the orbital period, but with a significant upper range. The radiative timescale, which is of similar scale to the rotation period, has a similarly large upper range, suggesting there is considerable degeneracy between the two timescales. The MCMC chain used to determine uncertainties remains quite close to the best-fit values in minimum temperature and albedo, while exploring an extended region of favorable likelihoods in projected parameter space for both rotation period and radiative timescale (Figure 5).

5.3.5. *WASP-12 b*

Due to the nature of the WASP-12 system, we expect limited success in effectively capturing the behavior of phase variations with a simple model. Prior to eclipse, the data in both bands exhibit very hot day-side temperatures; just prior to transit, the observed temperatures drop precipitously to a level which is effectively consistent with zero flux. Our models converge on results which prefer to cut through the rough median of the high-amplitude observations. Super-synchronous rotation rates produce pronounced phase offsets in each band; beyond this, our models fail to capture the extreme features in the photometry.

Among the first culprits possibly introducing second-order effects is the tidal distortion of the planet due to its proximity to its host star. We consider the effects of relaxing the spherical shape assumption for our planets in §A. Even with an ellipsoidal model with the appropriate ellipticity as determined by the mass ratio of the

² It should be noted that the 1σ range at $4.5 \mu\text{m}$ captures synchronous rotation; accordingly, the $4.5 \mu\text{m}$ photometry shows the weaker phase offset of the full-phase light curves.

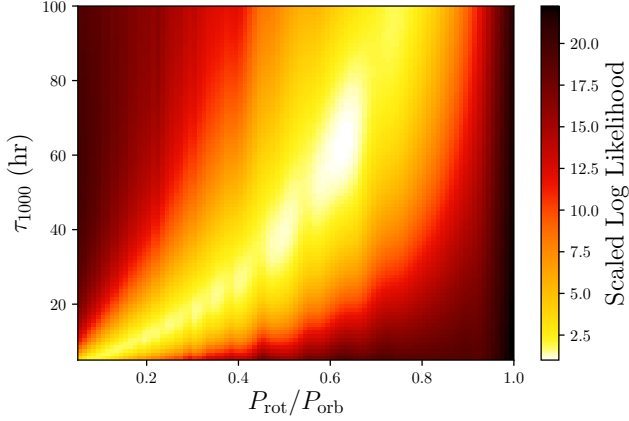


Figure 5. The 2D projection of likelihood space for the model of HD 209458b. The likelihoods are presented in logarithmic space, with unity fixed to the minimum likelihood. The most favorable likelihoods, shown in white, are not well-localized in one region but instead follow a track in the rotation period-radiative timescale plane. This is the primary contributor to the large 1σ uncertainties in both rotation period and radiative timescale.

system, the effect of including the distortion makes a negligible change in both the best-fit parameters and resulting model light curves (Figure 6).

5.3.6. WASP-14 b

While our models do a reasonable job of fitting the broad phase variations in each band, the photometry in both bands indicate that the total amplitudes might not be fully captured by our simple thermal model. In particular, the models capture the maxima well but unable to quite reach the minima, even with short radiative timescales.

5.3.7. WASP-18 b

In contrast with the results for WASP-14 b, here we are now unable to capture the peak fluxes, especially at $4.5 \mu\text{m}$, even with short radiative timescales, elevated minimum temperatures, and effectively complete absorption. Otherwise, the phase offsets in each band are minimal, leading to rotation periods roughly consistent with synchronous rotation.

5.3.8. WASP-19 b

Both models prefer rotation rates faster than synchronous, relatively fast radiative timescales, elevated night-side temperatures, and modest albedos. Across all parameters the 1σ bounds agree between 3.6 and $4.5 \mu\text{m}$, though the minima exhibit a similar case to the other WASP planets.

5.3.9. WASP-33 b

WASP-33 b has the lowest signal-to-noise ratio of all the WASP planets considered here. Nevertheless, the variations are largely fit by short radiative timescales, very high night-side temperatures, and significant albedos. The model rotation periods are in disagreement, but the pronouncement of the phase offsets is debatable given the quality of the data. Both photometric light curves show a strong drop-off just prior to transit, which the models do not capture.

5.3.10. WASP-43 b

Both models prefer rotation rates slightly faster than synchronous. The models disagree on the night-side temperature but with ambiguous cause. One reason for the seemingly inaccurate low night-side temperature at $3.6 \mu\text{m}$ might be due to a strange feature in the photometry following the eclipse. The flux drops off briefly, before returning to a level consistent with the rest of the phase variations³.

5.4. Eccentric Hot Jupiters

5.4.1. GJ 436 b

Our analyses are limited by the poor quality of the photometry, despite having in excess of one whole orbital period of observations. Our best results suggest the planet is rotating significantly faster than the eccentric pseudo-synchronous rate, which allows for a significant phase offset which is suggested by the observations prior to transit. The 1σ range in radiative timescales approach the rotation period at the upper limit, which likely serves to limit the amplitude of flux variations. The data never appear to settle close to unity, which is reflected in a range of night-side temperatures well above zero.

5.4.2. HAT-P-2 b

The results for 4.5 and $8.0 \mu\text{m}$ are consistent with pseudo-synchronous rotation, while the $3.6 \mu\text{m}$ model favors a slightly faster rotation. All radiative timescales suggest a response significantly faster than the expected rotation period, implying a small phase offset between peak flux and secondary eclipse, which is observed.

There is a strong disagreement in the minimum temperatures of the 3.6 and $8.0 \mu\text{m}$ models with that of the $4.5 \mu\text{m}$ model. This is not surprising given the data, which settles to a baseline flux ratio consistent with

³ Note that we have already excluded the data which were originally excluded in the original analysis presented in [Stevenson et al. \(2017\)](#). The feature we discuss here is one which persists in the published, included data.

zero planetary contribution for the $3.6\ \mu\text{m}$ data (and, arguably, the $8.0\ \mu\text{m}$ data prior to the peak), while remaining significantly higher than unity for the $4.5\ \mu\text{m}$ data. Under the assumption that the Spitzer photometry systematic uncertainties have been well characterized, this would imply that the observations probe different atmospheric layers depending on wavelength: a warm layer visible in the $4.5\ \mu\text{m}$ band, and a cooler layer in the others.

While the best fitting night-side temperature at $8.0\ \mu\text{m}$ is the lowest of all bands, we also at the same time fail to reach the peak observed flux in the band. Given that the available photometry only captures a single transit and eclipse, with the relatively short time separation between them, we are missing much of the orbital phases that constrain how the planet cools following periastron.

The observed eclipse depths are variable, particularly in 3.6 and $8.0\ \mu\text{m}$. In $3.6\ \mu\text{m}$, one eclipse depth is consistent with no planetary contribution to the flux, while the second is relatively elevated. For our analyses we phase-fold all photometry into a single orbit, thereby effectively folding these eclipses on top of one another. At $8.0\ \mu\text{m}$, while only one eclipse was observed in the partial-phase observation, the spread in the reduced data leads to binned median points below unity. This is an effect of the noise in the data.

This disagreement persists for albedo, with the 3.6 and $8.0\ \mu\text{m}$ models favoring effectively zero albedo (both with only modest upper limits), while the $4.5\ \mu\text{m}$ model favors a significant albedo of 0.42 .

Additionally, the observed transit depth is considerably different in 3.6 and $8.0\ \mu\text{m}$ from that in $4.5\ \mu\text{m}$. While wavelength-dependent opacity can contribute to differences in transit depths, from a scale height argument it is unlikely that a non-gray opacity would explain the difference. This is because of HAT-P-2 b’s high mass ($9.09\ M_J$) which would mitigate much of the differences in effective scale height. (See also the discussion in Section 4.4 of Lewis et al. (2013).)

5.4.3. HD 80606 b

HD 80606 b is in an extremely eccentric orbit ($e = 0.93366$) which brings into question the role of tidal heating and dissipation. Since HD 80606 b is thought to be the only planet in its system, and the age of its host star (and hence the system as a whole) is inconsistent with a young system ($\sim 1\text{--}10$ Gyr) (Takeda et al. 2007), the tidal Q must be $\gg 1$; in fact, de Wit et al. (2016) calculate this as $Q > 2.5 \times 10^6$. Therefore, the planet is expected to be extremely slow in both circularizing its orbit and speeding up its rotation.

Radiative timescales considerably shorter than the theoretical pseudo-synchronous rotation period of 39.9 hours allow the time of peak flux to be close enough to periastron. Each band requires a distinct, significant albedo to fit the observed maximum fluxes. While the best fits for the rotation period disagree, the uncertainties are among the largest of the planets we have considered. This is unsurprisingly almost certainly a consequence of the limited phase photometry for the planet, which also has by far the longest orbital period at 111 days. Our results therefore are at least marginally consistent with the published results from de Wit et al. (2016), who find a rotation period longer than pseudo-synchronous.

6. DISCUSSION

The existing full-orbit photometry from Spitzer are readily amenable to re-analysis using the simplest physically interesting radiative model. A blackbody model reproduces effectively the large-scale features in the data, capturing both the timescale of heating/cooling, time positions of minimum and maximum flux, and the depths of both transits and secondary eclipses.

The opportunity to study photometry in multiple wavelength bands allows us to compare the consistency of the model parameters. The most prevalent types of disagreements among bands of a single planet are those in night-side temperatures and albedos. The broadest explanation for these differences is that the photospheres for each wavelength are distinct, each having their own characteristic temperature and opacity. Arguably these properties are often among the most robustly determined from the data, since they arise almost entirely from the minima and amplitude of the phase variations. These disagreements show up in both high-eccentricity planets with multiple wavelengths, namely HAT-P-2 b and HD 80606 b. There is certainly the possibility of cloud formation due to the time-dependent instellation, that has a non-grey opacity.

For the majority of the planets studied here, the rotation period is not well-constrained observationally. Comparing the best-fit rotation periods among multiple planets, we note that there is a decently wide range of rotation periods. Acknowledging that many of our planets are strongly expected to have their solid-body rotation be synchronous with their orbital periods, the results suggest a range of coherent atmospheric motions. Eastward hot spots have been demonstrated for many Hot Jupiters on circular orbits, lending observational evidence for the existence of bulk equatorial flow of the atmospheric photosphere. The expectations for the characteristics of bulk flow for planets on eccentric orbits

are even less well-constrained. The primary challenge is the lack of full-orbit photometry available for eccentric Hot Jupiters; HAT-P-2 b is currently the only planet that meets this criterion. HAT-P-2 b will therefore be an interesting target for further observation to refine the constraints on its rotation and bulk atmospheric dynamics.

Beyond the possible astrophysical causes of variation among the model parameters, we have also discussed caution in over-interpreting the data currently available. There is a very real possibility that some number of observed features in the photometry are at least partially the result of uncharacterized systematic uncertainties. In the case of HAT-P-2 b, for example, there are two separate eclipse measurements whose fit depths have a slight overlap at 1σ but nevertheless disagree by roughly 20%. For some planets (e.g. HAT-P-2 b, HAT-P-7 b), the observed differences in transit depths is likely not entirely explained by predicted scale height differences in the atmosphere between photometric bands.

It is important to note that in many of the cases where fully 3D circulation models (GCMs) have been applied to partial and full phase photometry, they have been unable to fully explain the observed shape of the light curves. This is potentially due to physical phenom-

ena which have not been incorporated into the radiative transfer calculations. [Zellem et al. \(2014\)](#) speculate that the discrepancy in minimum night-side fluxes between the model s of [Showman et al. \(2009\)](#) and the observed light curve could, for example, be due to not modeling disequilibrium chemistry. In particular, a mechanism that could elevate CH_4 abundances in the atmosphere would provide a cooling source that could bring the theoretical night-side flux in $4.5 \mu\text{m}$ emission closer to the observed flux. In a more recent work, [Lewis et al. \(2017\)](#) apply similar GCMs to the periastron-centered photometry of HD 80606 b in an attempt to explain the observed shape and rate of heating in the 4.5 and $8.0 \mu\text{m}$ light curves.

As atmospheric detection and characterization moves forward with the anticipated launch of the James Webb Space Telescope, comprehensive characterization of the instrumental response and systematics will be crucial. The increased resolution alone will not be sufficient to disentangle the current ambiguities in exoplanet atmospheric data. Through careful target selection we hope to gather additional phase photometry that will aid in the determination of fundamental atmospheric properties, especially in the regime of high eccentricity.

APPENDIX

A. TIDAL DISTORTION: THE CASE OF WASP-12 B

WASP-12 b is very likely tidally distorted due to its density and proximity to its host star. Its radius ($1.83 R_J$) is quite inflated given its mass ($1.43 M_J$) ([Southworth 2012](#)), which suggests that the outermost layers of the planet’s atmosphere are susceptible to significant mass loss. [Li et al. \(2010\)](#) made the initial claim that WASP-12 b should be filling a significant part of its Roche lobe, a theoretical prediction that was expanded in subsequent works such as [Lai et al. \(2010\)](#).

One can use the ratio of the stellar and planetary masses to estimate the extent to which the planet’s shape should be distorted. The *Roche radius* describes the distance between the center of the planet and the $L1$ Lagrange point of the star-planet system:

$$\frac{R_{\text{Roche}}}{a} = \left(\frac{M_P}{3M_\star} \right)^{1/3} \quad (\text{A1})$$

For WASP-12 b, $R_{\text{Roche}}/R_P \approx 1.9$.

Given that WASP-12 b should be tidally distorted, one possible way to fit the observed light curves more accurately is to update the planet geometry in our model. To do this we assume the planet’s distorted shape may be approximately modeled as a prolate spheroid, whose prolate axis is assumed to always lie along the star-planet line. We define the “eccentricity” η of the elliptical cross-section of the planet along its prolate axis. That is, for semi-major and semi-minor axes A_P and B_P ,

$$\eta = \sqrt{1 - \left(\frac{B_P}{A_P} \right)^2}. \quad (\text{A2})$$

For planets whose radii are determined from transit depths, the measured radii R_P are equivalent to B_P , the semi-minor axes. This sets the axis ratio

$$\frac{A_P}{R_P} = (1 - \eta^2)^{-1/2}. \quad (\text{A3})$$

Li et al. (2010) estimate that the difference in observed emission flux from the planet between transit, where the minimum cross-sectional area is seen, and quadrature, where we see the maximum area, is of order $\sim 10\%$. This corresponds to a tidal eccentricity on order $\eta \sim 0.42$. This result can be accurately reproduced by solving for the maximum extent of the planet along each Cartesian axis, assuming those extreme points lie on the same surface of constant Jacobi energy, which is defined by

$$\begin{aligned} \Phi(\vec{x}) = -\frac{GM_\star}{a} & \left\{ \left[\left(\frac{x}{a} + \frac{\xi}{1+\xi} \right)^2 + \left(\frac{y}{a} \right)^2 + \left(\frac{z}{a} \right)^2 \right]^{-1/2} \right. \\ & + \left[\left(\frac{x}{a} + \frac{1}{1+\xi} \right)^2 + \left(\frac{y}{a} \right)^2 + \left(\frac{z}{a} \right)^2 \right]^{-1/2} \\ & \left. + \frac{1+\xi}{2} \left(\frac{x^2 + y^2}{a^2} \right) \right\} \end{aligned} \quad (\text{A4})$$

where ξ is the star-planet mass ratio M_P/M_\star , and the coordinates are set up such that x increases from star to planet, y points in the direction of the planet's motion in its orbit, and z is tangent to the orbital plane according to a right-handed coordinate system. The transit depth, calculated from observations, gives the product of the extent of the planet along the two dimensions normal to the star-planet axis (y and z)⁴.

The effect of the distortion on the area of each grid cell can be calculated using the first fundamental form. The surface of our planet can be parametrized in Cartesian coordinates as

$$\mathbf{r} = r_x \hat{x} + r_y \hat{y} + r_z \hat{z} \quad (\text{A5})$$

where

$$\begin{aligned} r_x &= A_P \cos \phi \sin \theta, \\ r_y &= B_P \sin \phi \sin \theta, \\ r_z &= B_P \cos \theta. \end{aligned}$$

The coordinates are defined as in Equation A4, with \hat{z} along the rotation axis and \hat{x} along the prolate (star-planet) axis.

In general, the area of an element on a solid surface is given as

$$A_{ij} = \int_{\phi_i}^{\phi_j} \int_{\theta_i}^{\theta_j} \sqrt{EG - F^2} d\theta d\phi \quad (\text{A6})$$

where

$$\begin{aligned} E &= \frac{d\mathbf{r}}{d\phi} \cdot \frac{d\mathbf{r}}{d\phi}, \\ F &= \frac{d\mathbf{r}}{d\phi} \cdot \frac{d\mathbf{r}}{d\theta}, \\ G &= \frac{d\mathbf{r}}{d\theta} \cdot \frac{d\mathbf{r}}{d\theta}. \end{aligned}$$

⁴ Note that solving this equation in general leads to different extents along y and z . For WASP-12 b, the differences are minor enough that the corresponding differences in calculated ellipticity are $\lesssim 0.01$.

The resulting integral becomes

$$A_{ij} = \frac{R_P^2}{1 - \eta^2} \int_{\phi_i}^{\phi_j} \int_{\theta_i}^{\theta_j} \sin \theta \left[1 - \eta^2 (2 - \cos^2 \theta) + \eta^4 (\sin^2 \theta + \cos^4 \theta \sin^2 \phi \cos^2 \phi) \right]^{1/2} d\theta d\phi. \quad (\text{A7})$$

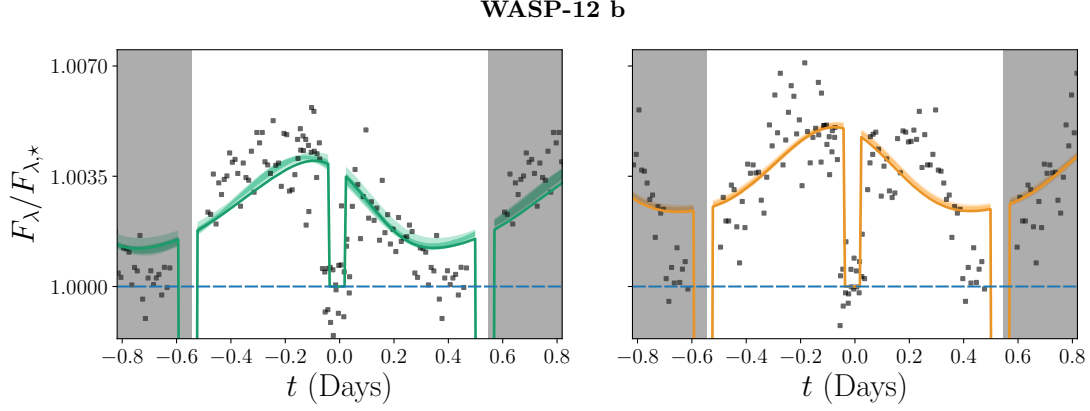


Figure 6. With a prolate eccentricity $\eta \approx 0.42$ (as defined and calculated from Equations A1–A4), we make little progress in how accurately our light curves reproduce the peak fluxes in the data.

B. TABLES OF ECLIPSE AND TRANSIT PROPERTIES

Table 4. Eclipse Properties for Exoplanets with Spitzer Light Curves

Band	E_{mid} (BJD – 2450000)	$E_{1,4}$ (days)	$E_{1,2} = E_{3,4}$ (days)	Depth	Ref.
GJ 436 b					
3.6 μm	4496.4888 ± 0.0010	0.0508 ± 0.0021		0.00041 ± 0.00003	Stevenson et al. (2010)
4.5 μm	4499.1330 ± 0.0010	0.0505 ± 0.0021		< 0.00010 (3σ)	Stevenson et al. (2010)
5.8 μm	4501.778 ± 0.005	0.0505 ± 0.0021		0.00033 ± 0.00014	Stevenson et al. (2010)
8.0 μm	4866.63444 ± 0.00082	0.04347	0.00700	0.000452 ± 0.000027	Knutson et al. (2011)
	4282.3331 ± 0.0016	0.0492 ± 0.0037		0.00054 ± 0.00008	Stevenson et al. (2010)
	$4282.33^{\text{H}} \pm 0.01$			0.00057 ± 0.00008	Deming et al. (2007)
16 μm	4477.981 ± 0.003	0.0505 ± 0.0061		0.00140 ± 0.00027	Stevenson et al. (2010)
24 μm	4470.053 ± 0.002	0.0505 ± 0.0061		0.00175 ± 0.00041	Stevenson et al. (2010)
HAT-P-2 b					
z	4388.546 ± 0.011	0.1650 ± 0.0034		0.00522 ± 0.00061	Pál et al. (2010)
3.6 μm	5289.9302 ± 0.0014	0.1550 ± 0.0027	0.01090 ± 0.00075	0.000996 ± 0.000072	Lewis et al. (2013)
4.5 μm	5757.5130 ± 0.0011	0.1651 ± 0.0023	0.01444 ± 0.00083	0.001031 ± 0.000061	Lewis et al. (2013)
5.8 μm	$4906.8561^{+0.0076}_{-0.0062}$			$0.00071^{+0.00029}_{-0.00013}$	Lewis et al. (2013)
8.0 μm	4354.7757 ± 0.0022	0.1610 ± 0.0043	0.0121 ± 0.0016	0.001392 ± 0.000095	Lewis et al. (2013)
HAT-P-7 b					
K_P				$6.930 \times 10^{-5} \pm 6 \times 10^{-7}$	Angerhausen et al. (2015)
3.6 μm	$5418.4562^{+0.0021}_{-0.0019}$			0.00156 ± 0.00009	Wong et al. (2016)

Table 4 continued

Table 4 (*continued*)

Band	E_{mid} (BJD - 2450000)	$E_{1,4}$ (days)	$E_{1,2} = E_{3,4}$ (days)	Depth	Ref.
4.5 μm	$5429.4780^{+0.0010}_{-0.0009}$			0.00190 ± 0.00006	Wong et al. (2016)
5.8 μm	4768.05200 ± 0.0035			0.00245 ± 0.00031	Christiansen et al. (2010)
8.0 μm	4770.26413 ± 0.0039			0.00225 ± 0.00052	Christiansen et al. (2010)
HD 80606 b					
$i/R_C/r/z$	$4424.736^{\text{H}} \pm 0.004$	0.0762 ± 0.0023	0.007188 ± 0.000263		Winn et al. (2009a)
4.5 μm				0.000651 ± 0.000049	de Wit et al. (2016)
8.0 μm				0.001053 ± 0.000094	de Wit et al. (2016)
	$4424.736^{\text{H}} \pm 0.003$	0.075 ± 0.010	0.005 ± 0.005	0.00136 ± 0.00018	Laughlin et al. (2009)
HD 149026 b					
3.6 μm	4535.8764 ± 0.0010	0.274 ± 0.002	0.0192 ± 0.0009	0.00040 ± 0.00003	Stevenson et al. (2012)
4.5 μm	4596.2676 ± 0.0019	0.274 ± 0.002	0.0195 ± 0.0010	0.00034 ± 0.00006	Stevenson et al. (2012)
5.8 μm	4903.990 ± 0.012	0.274 ± 0.002	0.0195 ± 0.0010	0.00044 ± 0.00010	Stevenson et al. (2012)
8.0 μm	4912.614 ± 0.002	0.274 ± 0.002	0.0195 ± 0.0010	0.00052 ± 0.00006	Stevenson et al. (2012)
HD 189733 b					
3.6 μm	$5560.66515^* \pm 0.00046$			0.001466 ± 0.000040	Knutson et al. (2012)
				0.00256 ± 0.00014	Charbonneau et al. (2008)
4.5 μm	$5187.94447^* \pm 0.00040$			0.001787 ± 0.000038	Knutson et al. (2012)
				0.00214 ± 0.00020	Charbonneau et al. (2008)
*	$2455560.66451 \pm 0.00025$				Knutson et al. (2012)
5.8 μm				0.00310 ± 0.00034	Charbonneau et al. (2008)
8.0 μm				0.00391 ± 0.00022	Charbonneau et al. (2008)
16 μm				0.00519 ± 0.00020	Charbonneau et al. (2008)
				0.00551 ± 0.00030	Deming et al. (2006)
24 μm				0.00598 ± 0.00038	Charbonneau et al. (2008)
HD 209458 b					
3.6 μm	$3702.5244^{\text{H}} \pm 0.0024$			0.00094 ± 0.00009	Knutson et al. (2008)
4.5 μm	$3702.5198^{\text{H}} \pm 0.0024$			0.00213 ± 0.00015	Knutson et al. (2008)
5.8 μm	$3702.5251^{\text{H}} \pm 0.0026$			0.00301 ± 0.00043	Knutson et al. (2008)
8.0 μm	$3702.5299^{\text{H}} \pm 0.0022$			0.00240 ± 0.00026	Knutson et al. (2008)
24 μm	$3346.5278^{\text{H}} \pm 0.0049$			0.00260 ± 0.00046	Deming et al. (2005)
WASP-12 b					
J				$0.00131^{+0.00027}_{-0.00029}$	Croll et al. (2011)
H				$0.00176^{+0.00016}_{-0.00051}$	Croll et al. (2011)
K_S				$0.00309^{+0.00013}_{-0.00012}$	Croll et al. (2011)
3.6 μm				0.00421 ± 0.00011	Stevenson et al. (2014)
				0.0038 ± 0.0004	Cowan et al. (2012)
	4773.6481 ± 0.0006	0.1229 ± 0.0012	0.0147	0.00379 ± 0.00013	Campo et al. (2011)
4.5 μm				0.00428 ± 0.00012	Stevenson et al. (2014)
				0.0039 ± 0.0003	Cowan et al. (2012)
	4769.2819 ± 0.0008	0.1244 ± 0.0017	0.0147	0.00382 ± 0.00019	Campo et al. (2011)
5.8 μm				0.00696 ± 0.0006	Stevenson et al. (2014)
	4773.6481 ± 0.0006	0.1229 ± 0.0012	0.0147	0.00629 ± 0.00052	Campo et al. (2011)
8.0 μm				0.00696 ± 0.00096	Stevenson et al. (2014)
	4769.2819 ± 0.0008	0.1244 ± 0.0017	0.0147	0.00636 ± 0.00067	Campo et al. (2011)

Table 4 *continued*

Table 4 (*continued*)

Band	E_{mid} (BJD $- 2450000$)	$E_{1,4}$ (days)	$E_{1,2} = E_{3,4}$ (days)	Depth	Ref.
WASP-14 b					
3.6 μm	5274.6617 ± 0.0006	0.1079 ± 0.0013	0.0121 ± 0.0003	0.00187 ± 0.00007	Blecic et al. (2013)
4.5 μm	4908.9298 ± 0.0011	0.1079 ± 0.0013	0.0121 ± 0.0003	0.00224 ± 0.00018	Blecic et al. (2013)
8.0 μm	4908.9298 ± 0.0011	0.1079 ± 0.0013	0.0121 ± 0.0003	0.00181 ± 0.00022	Blecic et al. (2013)
WASP-18 b					
3.6 μm	4820.7160 ± 0.0006	0.0944 ± 0.0007	0.0099	0.0030 ± 0.0002	Nymeyer et al. (2011)
4.5 μm	4824.4809 ± 0.0005	0.0944 ± 0.0007	0.0099	0.0039 ± 0.0002	Nymeyer et al. (2011)
5.8 μm	4820.7160 ± 0.0006	0.0944 ± 0.0007	0.0099	0.0037 ± 0.0003	Nymeyer et al. (2011)
8.0 μm	4824.4809 ± 0.0005	0.0944 ± 0.0007	0.0099	0.0041 ± 0.0002	Nymeyer et al. (2011)
WASP-19 b					
1.6–8.0 μm	$5183.56158^{+0.00042}_{-0.00035}$	$0.06564^{+0.00043}_{-0.00040}$	0.01358 ± 0.00054		Anderson et al. (2013)
2.09 μm				0.00366 ± 0.00067	Anderson et al. (2013)
3.6 μm	$5776.77019^{+0.00082}_{-0.00083}$			0.00485 ± 0.00024	Wong et al. (2016)
				0.00483 ± 0.00025	Anderson et al. (2013)
4.5 μm	$5787.02381^{+0.00078}_{-0.00076}$			0.00584 ± 0.00029	Wong et al. (2016)
				0.00572 ± 0.00030	Anderson et al. (2013)
5.8 μm				0.0065 ± 0.0011	Anderson et al. (2013)
8.0 μm				0.0073 ± 0.0012	Anderson et al. (2013)
WASP-33 b					
0.91 μm		0.11224 ± 0.00084	$0.01149^{+0.00097}_{-0.00084}$	0.00109 ± 0.00030	Smith et al. (2011)
K_s				$0.00244^{+0.00027}_{-0.00020}$	de Mooij et al. (2013)
	5844.8156 ± 0.0040			0.0027 ± 0.0004	Deming et al. (2012)
3.6 μm	5647.1978 ± 0.0001			0.0026 ± 0.0005	Deming et al. (2012)
4.5 μm	5650.8584 ± 0.0005			0.0041 ± 0.0002	Deming et al. (2012)
WASP-43 b					
TRAPPIST z' HAWK-I 1.19,					
2.09 μm	$5726.95069^{+0.00084}_{-0.00078}$	$0.05037^{+0.00023}_{-0.00021}$		$0.02542^{+0.00024}_{-0.00025}$	Gillon et al. (2012) Blecic et al. (2014),
3.6 μm	5773.3179 ± 0.0003	0.05208 ± 0.00083	0.01117 ± 0.00075	0.00323 ± 0.00006	Stevenson et al. (2017) Blecic et al. (2014),
4.5 μm	5772.5045 ± 0.0003	0.05208 ± 0.00083	0.01117 ± 0.00075	0.00383 ± 0.00008	Stevenson et al. (2017)

H_{T} Times are in HJD $- 2450000$.

* Knutson et al. (2012) report a combined secondary eclipse ephemeris.

NOTE—Times are in BJD $- 2450000$, unless otherwise noted.

Table 5. Transit Properties for Exoplanets with Spitzer Light Curves

Band	T_{mid} (BJD $- 2450000$)	$T_{1,4}$ (days)	$T_{1,2} = T_{3,4}$ (days)	Depth	Ref.
GJ 436 b					

Table 5 continued

Table 5 (continued)

Band	T_{mid} (BJD - 2450000)	$T_{1,4}$ (days)	$T_{1,2} = T_{3,4}$ (days)	Depth	Ref.
V				0.00696 ± 0.000117	Torres et al. (2008)
NICMOS	$4415.62074^{\text{H}} \pm 0.00008$				
1.1–1.9 μm	$4449.99141^{\text{H}} \pm 0.00008$	0.0317 ± 0.0004		0.006906 ± 0.000083	Pont et al. (2009)
H	$4534.59584^{\text{H}} \pm 0.00015$			0.00707 ± 0.00019	Alonso et al. (2008)
K_s	$4238.47898^{\text{H}} \pm 0.00046$			0.0064 ± 0.0003	Cáceres et al. (2009)
3.6 μm				0.006694 ± 0.000061	Knutson et al. (2011)
4.5 μm				0.006865 ± 0.000078	Knutson et al. (2011)
8.0 μm				0.006831 ± 0.000083	Knutson et al. (2011)
	$4280.78149^{\text{H}} \pm 0.00016$				Deming et al. (2007)
*	4865.083208 ± 0.000042	0.04227 ± 0.00016	0.01044 ± 0.00014	0.006907 ± 0.000043	Knutson et al. (2011)
HAT-P-2 b					
z	4387.43975 ± 0.00074	0.1787 ± 0.0013	$0.0141^{+0.0015}_{-0.0012}$	0.00522 ± 0.00061	Pál et al. (2010)
3.6 μm	5288.84988 ± 0.00060	0.1770 ± 0.0011	0.0128 ± 0.0010	0.004653 ± 0.000102	Lewis et al. (2013)
4.5 μm	5756.42520 ± 0.00067	0.1813 ± 0.0013	0.0177 ± 0.0012	0.004958 ± 0.000084	Lewis et al. (2013)
8.0 μm	4353.6911 ± 0.0012	0.1789 ± 0.0023	0.0144 ± 0.0021	0.004462 ± 0.000213	Lewis et al. (2013)
HAT-P-7 b					
i	$4731.67929^{\text{H}} \pm 0.00043$	0.1669 ± 0.0027	$0.0198^{+0.0025}_{-0.0039}$	0.0060202 ± 0.0000047	Winn et al. (2009b)
3.6 μm	$5419.55818^{+0.00054}_{-0.00070}$			$0.00629^{+0.00024}_{-0.00019}$	Wong et al. (2016)
4.5 μm	$5430.58278^{+0.00040}_{-0.00047}$			0.00604 ± 0.00012	Wong et al. (2016)
HD 80606 b					
$i/R_C/r/z$	$4987.7842^{\text{H}} \pm 0.0049$	0.4850 ± 0.0104	0.1083 ± 0.0075	0.01067 ± 0.00023	Winn et al. (2009a)
R	$4876.344^{\text{H}} \pm 0.011$			0.01117 ± 0.00038	Fossey et al. (2009)
HD 149026 b					
NICMOS	$4456.78761^{\text{H}} \pm 0.00014$	$0.270^{+0.012}_{-0.013}$	0.020 ± 0.001	$0.002933^{+0.000099}_{-0.000076}$	Carter et al. (2009)
8.0 μm	4597.70713 ± 0.00016	0.2738 ± 0.0016	0.0195 ± 0.0010	0.00268 ± 0.00006	Stevenson et al. (2012)
		$0.270^{+0.012}_{-0.013}$	0.019 ± 0.001	$0.002692^{+0.000087}_{-0.000089}$	Carter et al. (2009)
HD 189733 b					
3.6 μm	5559.554550 ± 0.000035			0.024059 ± 0.000062	Knutson et al. (2012)
4.5 μm	5189.052491 ± 0.000032			0.024274 ± 0.000059	Knutson et al. (2012)
8.0 μm	4279.436714 ± 0.000015	0.1789 ± 0.0023	0.0144 ± 0.0021	0.004462 ± 0.000213	Agol et al. (2010)
HD 209458 b					
290–1030 nm	$2826.628521^{\text{H}} \pm 0.000087$			0.014607 ± 0.000024	Knutson et al. (2007b)
**		0.13971 ± 0.00074	0.10027 ± 0.00068		Seager & Mallén-Ornelas (2003), Torres et al. (2008)
WASP-12 b					
B/z'	4508.9761 ± 0.0002	0.122 ± 0.001		0.0138 ± 0.0002	Hebb et al. (2009)
V	4508.97605 ± 0.00028	0.1666 ± 0.0015	0.0135 ± 0.0008	0.01252 ± 0.00045	Chan et al. (2012)
R	4508.97682 ± 0.00020	0.1220 ± 0.0010		0.01380 ± 0.00016	Maciejewski et al. (2011)
WASP-14 b					
$V + R, R, I$	$4463.57583^{\text{H}} \pm 0.00053$	$0.1275^{+0.0028}_{-0.0031}$		$0.0102^{+0.0002}_{-0.0003}$	Joshi et al. (2009)

Table 5 continued

Table 5 (*continued*)

Band	T_{mid} (BJD – 2450000)	$T_{1,4}$ (days)	$T_{1,2} = T_{3,4}$ (days)	Depth	Ref.
WASP-18 b					
HARPS	$4664.90531^{+0.00016}_{-0.00017}$	$0.09089^{+0.00080}_{-0.00061}$		$0.00916^{+0.00020}_{-0.00012}$	Triaud et al. (2010)
WASP-19 b					
r, z	$5183.16711^{\text{H}} \pm 0.000068$	0.06549 ± 0.00035	0.01346 ± 0.00052	0.02050 ± 0.00024	Anderson et al. (2013) , Hebb et al. (2010) , Hellier et al. (2011b)
$3.6 \mu\text{m}$	$5777.16364^{+0.00022}_{-0.00021}$			$0.01957^{+0.00039}_{-0.00050}$	Wong et al. (2016)
$4.5 \mu\text{m}$	$5787.41861^{+0.00023}_{-0.00022}$			$0.02036^{+0.00049}_{-0.00071}$	Wong et al. (2016)
WASP-33 b					
$R+I$, RV	$4163.22373^{\text{H}} \pm 0.00026$			0.01136 ± 0.00019	Collier Cameron et al. (2010)
Bessel U	2984.82964 ± 0.00030			$0.01179^{+0.00048}_{-0.00015}$	Turner et al. (2016)
$0.91 \mu\text{m}$	$4590.17948^{\text{H}} \pm 0.00028$	0.11224 ± 0.00084	$0.01149^{+0.00097}_{-0.00084}$	$0.01041^{+0.00023}_{-0.00021}$	Smith et al. (2011)
WASP-43 b					
TRAPPIST					
$I + z$,					
Gunn- r'	5726.54336 ± 0.00012	$0.05037^{+0.00023}_{-0.00021}$		$0.02542^{+0.00024}_{-0.00025}$	Gillon et al. (2012)
$3.6 \mu\text{m}$	7089.11181 ± 0.00007			0.02496 ± 0.00010	Stevenson et al. (2017)
$4.5 \mu\text{m}$	6897.13195 ± 0.00007			0.02525 ± 0.00016	Stevenson et al. (2017)

H_{Times} are in HJD–2450000.

* Transit properties are from combined wavelength fits.

** Transit duration and ingress/egress times are calculated from the geometric relation described in [Seager & Mallén-Ornelas \(2003\)](#), using the transit properties in [Torres et al. \(2008\)](#).

NOTE—Times are in BJD–2450000, unless otherwise noted. Where the source authors specify times with respect to the UTC and TDB systems ([Eastman et al. 2010](#)), we choose to quote the TDB time.

Acknowledgements go here.

Facility: Spitzer (IRAC)

Software: Astropy ([Astropy Collaboration et al. 2013](#)), Matplotlib ([Hunter 2007](#)), Numpy ([van der Walt et al. 2011](#)), WebPlotDigitizer ([Rohatgi 2017](#))

REFERENCES

- Agol, E., Cowan, N. B., Knutson, H. A., Deming, D., Steffen, J. H., Henry, G. W., & Charbonneau, D. 2010, *ApJ*, 721, 1861
- Albrecht, S. et al. 2012, *ApJ*, 757, 18
- Alonso, R., Barbieri, M., Rabus, M., Deeg, H. J., Belmonte, J. A., & Almenara, J. M. 2008, *A&A*, 487, L5
- Amundsen, D. S. et al. 2016, *A&A*, 595, A36
- Anderson, D. R. et al. 2013, *MNRAS*, 430, 3422
- Angerhausen, D., DeLarme, E., & Morse, J. A. 2015, *PASP*, 127, 1113
- Armstrong, D. J., de Mooij, E., Barstow, J., Osborn, H. P., Blake, J., & Fereshteh Saniee, N. 2016, *ArXiv e-prints*
- Astropy Collaboration et al. 2013, *A&A*, 558, A33
- Baluev, R. V. et al. 2015, *MNRAS*, 450, 3101
- Baskin, N. J. et al. 2013, *ApJ*, 773, 124
- Beaulieu, J. P. et al. 2010, *MNRAS*, 409, 963
- Beichman, C. et al. 2014, *PASP*, 126, 1134
- Berta, Z. K. et al. 2012, *ApJ*, 747, 35
- Blecic, J. et al. 2014, *ApJ*, 781, 116
- . 2013, *ApJ*, 779, 5
- Boyajian, T. et al. 2015, *MNRAS*, 447, 846
- Burrows, A., Budaj, J., & Hubeny, I. 2008, *ApJ*, 678, 1436
- Cáceres, C., Ivanov, V. D., Minniti, D., Naef, D., Melo, C., Mason, E., Selman, F., & Pietrzynski, G. 2009, *A&A*, 507, 481
- Campo, C. J. et al. 2011, *ApJ*, 727, 125
- Carey, S. et al. 2012, in *Proc. SPIE*, Vol. 8442, *Space Telescopes and Instrumentation 2012: Optical, Infrared, and Millimeter Wave*, 84421Z
- Carter, J. A., Winn, J. N., Gilliland, R., & Holman, M. J. 2009, *ApJ*, 696, 241
- Chan, T., Ingemr, M., Winn, J. N., Holman, M. J., Sanchis-Ojeda, R., Esquerdo, G., & Everett, M. 2012, *The Astronomical Journal*, 144, 90
- Charbonneau, D., Knutson, H. A., Barman, T., Allen, L. E., Mayor, M., Megeath, S. T., Queloz, D., & Udry, S. 2008, *ApJ*, 686, 1341
- Christiansen, J. L. et al. 2010, *ApJ*, 710, 97
- Collier Cameron, A. et al. 2010, *MNRAS*, 407, 507
- Cowan, N. B., & Agol, E. 2008, *ApJL*, 678, L129
- . 2011, *ApJ*, 729, 54
- Cowan, N. B., Machalek, P., Croll, B., Shekhtman, L. M., Burrows, A., Deming, D., Greene, T., & Hora, J. L. 2012, *ApJ*, 747, 82
- Croll, B., Lafreniere, D., Albert, L., Jayawardhana, R., Fortney, J. J., & Murray, N. 2011, *AJ*, 141, 30
- Crossfield, I. J. M., Barman, T., Hansen, B. M. S., & Howard, A. W. 2013, *A&A*, 559, A33
- Crossfield, I. J. M., Knutson, H., Fortney, J., Showman, A. P., Cowan, N. B., & Deming, D. 2012, *ApJ*, 752, 81
- Crouzet, N., McCullough, P. R., Deming, D., & Madhusudhan, N. 2014, *ApJ*, 795, 166
- de Kok, R. J., Brogi, M., Snellen, I. A. G., Birkby, J., Albrecht, S., & de Mooij, E. J. W. 2013, *A&A*, 554, A82
- de Mooij, E. J. W., Brogi, M., de Kok, R. J., Snellen, I. A. G., Kenworthy, M. A., & Karjalainen, R. 2013, *A&A*, 550, A54
- de Wit, J., Gillon, M., Demory, B.-O., & Seager, S. 2012, *A&A*, 548, A128
- de Wit, J., Lewis, N. K., Langton, J., Laughlin, G., Deming, D., Batygin, K., & Fortney, J. J. 2016, *ApJL*, 820, L33
- Deming, D. et al. 2012, *ApJ*, 754, 106
- Deming, D., Harrington, J., Laughlin, G., Seager, S., Navarro, S. B., Bowman, W. C., & Horning, K. 2007, *The Astrophysical Journal Letters*, 667, L199
- Deming, D., Harrington, J., Seager, S., & Richardson, L. J. 2006, *ApJ*, 644, 560
- Deming, D., Seager, S., Richardson, L. J., & Harrington, J. 2005, *Nature*, 434, 740
- Désert, J.-M., Lecavelier des Etangs, A., Hébrard, G., Sing, D. K., Ehrenreich, D., Ferlet, R., & Vidal-Madjar, A. 2009, *ApJ*, 699, 478
- Diamond-Lowe, H., Stevenson, K. B., Bean, J. L., Line, M. R., & Fortney, J. J. 2014, *ApJ*, 796, 66
- Dobbs-Dixon, I., & Agol, E. 2013, *MNRAS*, 435, 3159
- Eastman, J., Siverd, R., & Gaudi, B. S. 2010, *PASP*, 122, 935
- Eggleton, P. P., & Kiseleva-Eggleton, L. 2001, *ApJ*, 562, 1012
- Enoch, B., Collier Cameron, A., Parley, N. R., & Hebb, L. 2010, *A&A*, 516, A33
- Evans, T. M. et al. 2013, *ApJL*, 772, L16
- Fabrycky, D., & Tremaine, S. 2007, *ApJ*, 669, 1298
- Fortney, J. J., Lodders, K., Marley, M. S., & Freedman, R. S. 2008, *ApJ*, 678, 1419
- Fossey, S. J., Waldmann, I. P., & Kipping, D. M. 2009, *Monthly Notices of the Royal Astronomical Society: Letters*, 396, L16
- Gillon, M. et al. 2012, *A&A*, 542, A4
- Goldreich, P., & Soter, S. 1966, *Icarus*, 5, 375
- Grillmair, C. J., Charbonneau, D., Burrows, A., Armus, L., Stauffer, J., Meadows, V., Van Cleve, J., & Levine, D. 2007, *ApJL*, 658, L115
- Hansen, C. J., Schwartz, J. C., & Cowan, N. B. 2014, *MNRAS*, 444, 3632
- Hebb, L. et al. 2009, *ApJ*, 693, 1920
- . 2010, *ApJ*, 708, 224

- Hébrard, G. et al. 2010, *A&A*, 516, A95
- Hellier, C. et al. 2011a, *A&A*, 535, L7
- Hellier, C., Anderson, D. R., Collier-Cameron, A., Miller, G. R. M., Queloz, D., Smalley, B., Southworth, J., & Triaud, A. H. M. J. 2011b, *ApJL*, 730, L31
- Houck, J. R. et al. 2004, *ApJS*, 154, 18
- Huitson, C. M., Sing, D. K., Vidal-Madjar, A., Ballester, G. E., Lecavelier des Etangs, A., Désert, J.-M., & Pont, F. 2012, *MNRAS*, 422, 2477
- Hunter, J. D. 2007, *Computing in Science Engineering*, 9, 90
- Hut, P. 1981, *A&A*, 99, 126
- Ingalls, J. G. et al. 2016, *AJ*, 152, 44
- Johnson, J. A., Winn, J. N., Albrecht, S., Howard, A. W., Marcy, G. W., & Gazak, J. Z. 2009, *PASP*, 121, 1104
- Joshi, Y. C. et al. 2009, *MNRAS*, 392, 1532
- Kataria, T., Showman, A. P., Fortney, J. J., Stevenson, K. B., Line, M. R., Kreidberg, L., Bean, J. L., & Désert, J.-M. 2015, *ApJ*, 801, 86
- Knutson, H. A., Charbonneau, D., Allen, L. E., Burrows, A., & Megeath, S. T. 2008, *ApJ*, 673, 526
- Knutson, H. A. et al. 2007a, *Nature*, 447, 183
- Knutson, H. A., Charbonneau, D., Cowan, N. B., Fortney, J. J., Showman, A. P., Agol, E., & Henry, G. W. 2009, *The Astrophysical Journal*, 703, 769
- Knutson, H. A. et al. 2009, *ApJ*, 690, 822
- Knutson, H. A., Charbonneau, D., Noyes, R. W., Brown, T. M., & Gilliland, R. L. 2007b, *ApJ*, 655, 564
- Knutson, H. A. et al. 2014, *ApJ*, 785, 126
- Knutson, H. A., Howard, A. W., & Isaacson, H. 2010, *ApJ*, 720, 1569
- Knutson, H. A. et al. 2012, *ApJ*, 754, 22
- . 2011, *ApJ*, 735, 27
- Komacek, T. D., & Showman, A. P. 2016, *ApJ*, 821, 16
- Kozai, Y. 1962, *AJ*, 67, 591
- Lai, D., Helling, C., & van den Heuvel, E. P. J. 2010, *ApJ*, 721, 923
- Lainey, V., Arlot, J.-E., Karatekin, Ö., & van Hoolst, T. 2009, *Nature*, 459, 957
- Lanotte, A. A. et al. 2014, *A&A*, 572, A73
- Laughlin, G., Deming, D., Langton, J., Kasen, D., Vogt, S., Butler, P., Rivera, E., & Meschiari, S. 2009, *Nature*, 457, 562
- Lewis, N. K. et al. 2013, *ApJ*, 766, 95
- Lewis, N. K., Parmentier, V., Kataria, T., de Wit, J., Showman, A. P., Fortney, J. J., & Marley, M. S. 2017, *ArXiv e-prints*
- Lewis, N. K., Showman, A. P., Fortney, J. J., Knutson, H. A., & Marley, M. S. 2014, *ApJ*, 795, 150
- Lewis, N. K., Showman, A. P., Fortney, J. J., Marley, M. S., Freedman, R. S., & Lodders, K. 2010, *ApJ*, 720, 344
- Li, S.-L., Miller, N., Lin, D. N. C., & Fortney, J. J. 2010, *Nature*, 463, 1054
- Lidov, M. L. 1962, *Planet. Space Sci.*, 9, 719
- Line, M. R. et al. 2016, *AJ*, 152, 203
- Maciejewski, G., Errmann, R., Raetz, S., Seeliger, M., Spaleniak, I., & Neuhäuser, R. 2011, *A&A*, 528, A65
- Maciejewski, G., Niedzielski, A., Nowak, G., Pallé, E., Tingley, B., Errmann, R., & Neuhäuser, R. 2014, *AcA*, 64, 323
- Madhusudhan, N. 2012, *ApJ*, 758, 36
- Madhusudhan, N. et al. 2011, *Nature*, 469, 64
- Madhusudhan, N., & Seager, S. 2009, *ApJ*, 707, 24
- . 2010, *ApJ*, 725, 261
- Mahtani, D. P. et al. 2013, *MNRAS*, 432, 693
- Majeau, C., Agol, E., & Cowan, N. B. 2012, *ApJL*, 747, L20
- Mandell, A. M., Haynes, K., Sinukoff, E., Madhusudhan, N., Burrows, A., & Deming, D. 2013, *ApJ*, 779, 128
- Maxted, P. F. L. et al. 2013, *MNRAS*, 428, 2645
- Millholland, S., & Laughlin, G. 2017, *AJ*, 154, 83
- Moutou, C. et al. 2009, *A&A*, 498, L5
- Nymeyer, S. et al. 2011, *ApJ*, 742, 35
- O’Rourke, J. G. et al. 2014, *The Astrophysical Journal*, 781, 109
- Pál, A. et al. 2010, *MNRAS*, 401, 2665
- . 2008, *ApJ*, 680, 1450
- Pont, F., Gilliland, R. L., Knutson, H., Holman, M., & Charbonneau, D. 2009, *MNRAS*, 393, L6
- Raetz, S. et al. 2015, *MNRAS*, 451, 4139
- Rasio, F. A., Tout, C. A., Lubow, S. H., & Livio, M. 1996, *ApJ*, 470, 1187
- Rauscher, E., Menou, K., Cho, J. Y.-K., Seager, S., & Hansen, B. M. S. 2007, *The Astrophysical Journal Letters*, 662, L115
- Rieke, G. H. et al. 2004, *ApJS*, 154, 25
- Rodler, F., Kürster, M., & Barnes, J. R. 2013, *MNRAS*, 432, 1980
- Rohatgi, A. 2017, *WebPlotDigitizer*, <https://automeris.io/WebPlotDigitizer>
- Salz, M., Schneider, P. C., Czesla, S., & Schmitt, J. H. M. M. 2015, *A&A*, 576, A42
- Schwartz, J. C., & Cowan, N. B. 2015, *MNRAS*, 449, 4192
- Schwarz, H., Brogi, M., de Kok, R., Birkby, J., & Snellen, I. 2015, *A&A*, 576, A111
- Seager, S., & Mallén-Ornelas, G. 2003, *ApJ*, 585, 1038
- Showman, A. P., Fortney, J. J., Lian, Y., Marley, M. S., Freedman, R. S., Knutson, H. A., & Charbonneau, D. 2009, *ApJ*, 699, 564
- Showman, A. P., & Guillot, T. 2002, *A&A*, 385, 166

- Showman, A. P., Lewis, N. K., & Fortney, J. J. 2015, *ApJ*, 801, 95
- Shporer, A. 2017, *PASP*, 129, 072001
- Smith, A. M. S., Anderson, D. R., Skillen, I., Collier Cameron, A., & Smalley, B. 2011, *MNRAS*, 416, 2096
- Snellen, I. A. G., de Kok, R. J., de Mooij, E. J. W., & Albrecht, S. 2010, *Nature*, 465, 1049
- Southworth, J. 2010, *MNRAS*, 408, 1689
- . 2012, *MNRAS*, 426, 1291
- Stevenson, K. B., Bean, J. L., Madhusudhan, N., & Harrington, J. 2014, *ApJ*, 791, 36
- Stevenson, K. B. et al. 2012, *ApJ*, 754, 136
- . 2010, *Nature*, 464, 1161
- . 2017, *AJ*, 153, 68
- Takeda, G., Ford, E. B., Sills, A., Rasio, F. A., Fischer, D. A., & Valenti, J. A. 2007, *ApJS*, 168, 297
- Todorov, K., Deming, D., Harrington, J., Stevenson, K. B., Bowman, W. C., Nymeyer, S., Fortney, J. J., & Bakos, G. A. 2010, *ApJ*, 708, 498
- Todorov, K. O., Deming, D., Burrows, A., & Grillmair, C. J. 2014, *ApJ*, 796, 100
- Todorov, K. O. et al. 2013, *ApJ*, 770, 102
- Torres, G., Fischer, D. A., Sozzetti, A., Buchhave, L. A., Winn, J. N., Holman, M. J., & Carter, J. A. 2012, *ApJ*, 757, 161
- Torres, G., Winn, J. N., & Holman, M. J. 2008, *ApJ*, 677, 1324
- Tregloan-Reed, J., Southworth, J., & Tappert, C. 2013, *MNRAS*, 428, 3671
- Triaud, A. H. M. J. et al. 2010, *A&A*, 524, A25
- Triaud, A. H. M. J., Lanotte, A. A., Smalley, B., & Gillon, M. 2014, *MNRAS*, 444, 711
- Triaud, A. H. M. J. et al. 2009, *A&A*, 506, 377
- Turner, J. D. et al. 2016, *MNRAS*, 459, 789
- van der Walt, S., Colbert, S. C., & Varoquaux, G. 2011, *Computing in Science Engineering*, 13, 22
- von Braun, K. et al. 2012, *ApJ*, 753, 171
- von Paris, P., Gratier, P., Bordé, P., & Selsis, F. 2016, *A&A*, 587, A149
- Werner, M. 2006, in *Astronomical Society of the Pacific Conference Series*, Vol. 357, *Astronomical Society of the Pacific Conference Series*, ed. L. Armus & W. T. Reach, 7
- Werner, M. W. et al. 2004, *ApJS*, 154, 1
- Winn, J. N. et al. 2009a, *ApJ*, 703, 2091
- Winn, J. N., Johnson, J. A., Albrecht, S., Howard, A. W., Marcy, G. W., Crossfield, I. J., & Holman, M. J. 2009b, *ApJL*, 703, L99
- Winn, J. N. et al. 2005, *ApJ*, 631, 1215
- Wong, I. et al. 2014, *ApJ*, 794, 134
- . 2016, *ApJ*, 823, 122
- . 2015, *ApJ*, 811, 122
- Wu, Y., & Murray, N. 2003, *ApJ*, 589, 605
- Zellem, R. T. et al. 2014, *ApJ*, 790, 53
- Zhang, M. et al. 2017, *ArXiv e-prints*